Investigating the Feasibility of 3D Printed Pressure Taps for Surface Pressure Measurements in Wind Tunnel

by

Sahaj Thapa

Submitted in Partial Fulfillment of the Requirements

for the Degree of

Master of Science in Engineering

in

Mechanical Engineering

YOUNGSTOWN STATE UNIVERSITY

May, 2023

Investigating the Feasibility of 3D Printed Pressure Taps for Surface Pressure Measurements in Wind Tunnel

Sahaj Thapa

I hereby release this thesis to the public. I understand that this thesis will be made available from the OhioLINK ETD Center and the Maag Library Circulation Desk for public access. I also authorize the University or other individuals to make copies of this thesis as needed for scholarly research.

Signature:

_____

Sahaj Thapa, Student Date

Approvals:

_____

Dr. Stefan Moldovan, Thesis Advisor Date

_____

Dr. *C. Virgil Solomon*, Committee Member Date

_____

Dr. Kyosung Choo, Committee Member Date

_____

Salvatore A. Sanders, PhD, Dean, College of Graduate Studies Date

Abstract

Pressure taps are commonly used in aerodynamics to measure the pressure distribution on the surface of objects in air flow and provide valuable information for the analysis of aerodynamic performance. However, traditional pressure tap technology has limitations in terms of customization and complexity, making it difficult to measure pressure in certain regions or with certain geometries. This has led to a growing interest in using 3D printing technology to produce pressure taps, as it allows for the creation of complex and customized components. This research aimed to investigate the feasibility of using 3D printed pressure taps for surface pressure measurements in aerodynamics and compare their performance with conventional pressure taps. The study included designing and producing 3D printed pressure taps with intricate and customized shapes for airfoils and cylinders, evaluating their performance in terms of accuracy and precision. The study also investigated the potential limitations and challenges associated with using 3D printed pressure taps and developed strategies to overcome these limitations.

The experimental methodology involved exploring the design of a cylinder and a NACA 2412 airfoil with and without vortex generators. The study found that the pressure coefficients in flow around cylinder for the straight and complex path cases were similar, with the differences being within the expected range of experimental error. The 3D printed pressure taps were effective in capturing the complex flow features around the airfoil, including the effects of vortex generators installed on the airfoil. Moreover, the experimental findings exhibited a high degree of concurrence with the computational fluid dynamics (CFD) simulation outcomes. The comparison of experimental and literature data

revealed the typical characteristics of flow, including a separation and a gradual increase in Cp before the onset of vortex shedding.

The study demonstrated the potential of 3D printing technology to produce complex shapes with embedded pressure taps for reliable flow measurement. The study also validated the use of 3D printed cylinders and airfoils with embedded pressure taps for experimental investigation of flow behavior, which can be relied upon for further analysis. The findings provide useful insights into the flow behavior around cylinders and airfoils, which can be applied in the design and optimization of aerodynamic structures. Overall, this study contributes to the development of 3D printing technology for aerodynamic research and provides new insights and recommendations for the design and use of 3D printed pressure taps in aerodynamics.

Acknowledgments

I am deeply grateful to my thesis advisor, Dr. Stephen Moldovan, for his invaluable guidance, support, and encouragement throughout my graduate studies. His along with my committee members, Dr. Virgil Solomon and Dr. Kyosung Choo expertise, insight, and constructive feedback have been instrumental in shaping my research and refining my analytical and critical thinking skills. I would also like to thank Dr. Kevin Disotell for shaping my academic career and instilling in me a passion for research.

I would like to extend my sincere gratitude to Eric Haake, whose tireless dedication, technical expertise, and collaboration have been essential to the success of this project. His contributions to the design and experimental setup have been invaluable. Also, thanks to Brandon Malahtaris for his inputs on FDM prints.

In addition, I would like to thank my colleagues for their support, stimulating discussions, and camaraderie. Additionally, I would like to acknowledge the financial support provided by the Cushwa/Commercial Shearing Graduate Fellowship, which has enabled me to pursue my research interests.

Finally, I am immensely grateful to my parents Hutaraj, Sajana and my brother, Swochhanda for their support and being my constant source of inspiration and motivation. Akankshya, your love, companionship and unwavering belief in my abilities have been my refuge throughout this whole journey. I will see you soon.

Table of Contents

List of Figures

List of Tables

Nomenclature

C	Airfoil chord length
C_L	Lift Coefficient
C_D	Drag Coefficient
Cp	Pressure Coefficient
L	Characteristics Length Scale
ρ	Density of air
μ	Dynamic viscosity of air
α	Angle of attack
δ	Boundary Layer height
P	Local static Pressure
2-D	Two-Dimensional
CFD	Computational Fluid Dynamics
CNC	Computer Numerical Control
NACA	National Advisory Committee for Aeronautics
PIV	Particle Image Velocimetry
RMS	Root Mean Square
RANS	Reynolds Averaged Navier-Stokes
YSU	Youngstown State University

CHAPTER 1. INTRODUCTION

1.1. Overview of Additive Manufacturing

Aerodynamics plays a critical role in engineering by examining the flow of air and forces developed around objects in motion, such as aircrafts, vehicles, and helicopters. The aerodynamic forces that act upon these objects greatly impact their performance, making it necessary to have precise and dependable methods for measuring them. Pressure taps are commonly used in aerodynamics to measure the pressure on the surface of objects in air flow and provide essential data for analyzing aerodynamic performance.

3D printing technology, also known as additive manufacturing, has been increasingly used in various industries, including aerospace engineering. In aerodynamic studies, 3D printing enables the rapid and cost-effective production of models of prototype models which can then be tested in wind tunnels to measure their performance. Additionally, the technology allows for the creation of complex geometries that would be difficult or impossible to manufacture using traditional methods, providing new possibilities for innovative aerodynamic designs. The use of 3D printing in aerodynamic studies can improve the design process, and ultimately lead to more efficient and effective aircrafts. With the advancement of 3D printing, the utilization of 3D printed pressure taps is becoming a potential replacement for conventional pressure taps.

1.2 Motivation

Pressure taps are commonly used in aerodynamics to measure the pressure distribution on the surface of objects in air flow and provide valuable information for the analysis of aerodynamic performance. However, traditional pressure tap technology has

limitations in terms of customization and complexity, making it difficult to measure pressure in certain regions or with certain geometries. This has led to a growing interest in using 3D printing technology to produce pressure taps, as it allows for the creation of complex and customized components. The use of 3D printed pressure taps offers a promising alternative to conventional pressure tap technology, as it can be tailored to meet specific measurement requirements. The use of 3D printed pressure taps offers several advantages over conventional pressure taps. Customization is one of the main advantages of 3D printing technology since it makes it possible to produce pressure taps with intricate and unique designs that may be blended into complicated geometric shapes. This is particularly useful in regions that are difficult to access with conventional pressure taps. This results in increased accuracy and precision in pressure measurements, leading to more reliable and dependable results. The ability to produce complex and customized pressure taps at a lower cost than traditional manufacturing methods is another major advantage of 3D printing technology, as it can help reduce costs in the aerodynamic testing process. Furthermore, 3D printed pressure taps can lead to increased efficiency in the aerodynamic testing process, as they can be designed and produced faster and with fewer production errors compared to conventional pressure taps.

The motivation behind this research is to investigate the feasibility of using 3D printed pressure taps for surface pressure measurements in aerodynamics. The study aims to demonstrate the potential of 3D printing technology in the field of aerodynamics and provide new insights into the use of 3D printed pressure taps for surface pressure measurements. The findings of this study have the potential to lead to the development of new and improved pressure tap designs, which can help in advancing the field of

experimental aerodynamics and improving the performance of objects in motion. The study is motivated by the desire to explore the benefits and limitations of using 3D printed pressure taps in aerodynamics and to contribute to the field by providing new and valuable information. Additionally, this research aims to explore the effectiveness of 3D printed pressure taps on vortical flows by incorporating vortex generators on an airfoil and measuring surface pressure using the printed taps. The ability to accurately measure surface pressure in vortical flows is crucial for understanding and optimizing flow control strategies, and 3D printing offers the potential for intricate and customized pressure tap designs. By evaluating the performance of 3D printed pressure taps on vortical flows, this research seeks to contribute to the development of new and improved pressure tap designs for aerodynamic applications.

1.3 Research Objectives

The main objective of this research is to investigate the feasibility of using 3D printed pressure taps for surface pressure measurements in aerodynamics and to compare their performance with conventional pressure taps. The specific objectives are as follows:

1. To design and produce 3D printed pressure taps with intricate and customized shapes used on airfoils and cylinders that can show the capabilities of this technique.
2. To evaluate the accuracy and precision of 3D printed pressure taps in measuring surface pressure in aerodynamics.
3. To compare the performance of 3D printed pressure taps with conventional pressure taps in terms of accuracy, precision, and cost-effectiveness.
4. To investigate the potential limitations and challenges associated with using 3D printed pressure taps in aerodynamics and to develop strategies to overcome these limitations.

5. To provide new insights and recommendations for the design and use of 3D printed pressure taps in aerodynamics.
6. To investigate the feasibility and effectiveness of 3D printed pressure taps in measuring surface pressure in vortical flows, using vortex generators on airfoils as an application.

The research will be conducted by designing and producing 3D printed pressure taps, conducting wind tunnel tests to measure surface pressure, and comparing the results with conventional pressure taps. Data analysis will be performed to evaluate the accuracy and precision of 3D printed pressure taps and to compare their performance with conventional pressure taps. The findings of this study will contribute to the field of aerodynamics by providing new insights into the use of 3D printed pressure taps for surface pressure measurements and developing new and improved pressure tap designs.

CHAPTER 2. LITERATURE REVIEW

Rapid prototyping and pressure tap technology are two key areas of focus in the field of product development and aerodynamics testing, respectively. The use of rapid prototyping methods such as 3D printing, stereolithography, and selective laser sintering has revolutionized the product development process by allowing for rapid iteration and improvements to be made in a fraction of the time and cost compared to traditional manufacturing methods. Similarly, pressure tap technology has evolved over time, providing valuable information about the flow characteristics of aerodynamic objects and aiding in the design, analysis, and optimization of their performance. The combination of these two fields has recently been explored, and studies have shown that rapid prototyping methods can be used to produce wind-tunnel models with comparable aerodynamic characteristics to those produced using traditional methods, but with the added benefits of reduced lead time and cost, improved design freedom, and the ability to quickly produce multiple iterations of a design. The aim of this chapter is to provide a comprehensive review of the literature on both rapid prototyping and pressure tap technology, highlighting their significance, methods, and applications in the field of product development and aerodynamics testing.

2.1. Rapid Prototyping (RP)

Rapid prototyping refers to a set of methods and technologies used to quickly manufacture a scale model of a physical product. The primary objective of rapid prototyping is to allow designers and engineers to test and evaluate a product's design,

performance and fit before committing to full-scale production. This process has revolutionized the way products are developed, as it allows for rapid iteration and improvements to be made in a fraction of the time and cost compared to traditional manufacturing methods. Rapid prototyping techniques, such as 3D printing, stereolithography, and selective laser sintering, are used to produce functional prototypes made from plastic, metal, or other materials. This process has increased the speed of innovation in a wide range of industries, from consumer goods to aerospace and healthcare. Rapid prototyping has become an essential tool in the product development process, allowing companies to bring their ideas to market faster and more effectively.

There are several types of rapid prototyping, each with its own unique set of advantages and limitations. Some of the most common types of rapid prototyping include [1]:

1. 3D Printing: This is a process where a 3D model is created by layering material, such as plastic or metal, to create a physical product.
2. Stereolithography (SLA): This is a process where a 3D model is created by curing a photopolymer resin with a UV laser to produce a solid object.
3. Selective Laser Sintering (SLS): This is a process where a laser is used to fuse particles of plastic, metal, or ceramic into a solid object.
4. Fused Deposition Modeling (FDM): This is a process where a melted material is deposited in layers to build a 3D object.
5. Laminated Object Manufacturing (LOM): This is a process where layers of material, such as paper or plastic, are glued together and then cut to create a 3D object.

6. CNC Machining: This is a process where a material is removed from a block using a computer-controlled cutting tool to create a 3D object.

In terms of materials, there are many options available for 3D printing. Thermoplastics, such as PLA and ABS, are the most commonly used materials due to their affordability and ease of use. Other materials, such as nylon and polycarbonate, offer improved strength and durability but require higher printing temperatures and more advanced printers. Additionally, there are specialty materials like metal powders and ceramics that can be 3D printed but require specialized equipment and processes.

2.2. Pressure Tap Technology in Aerodynamics

Pressure taps are an essential component of aerodynamic testing, providing valuable information about the flow characteristics of aircrafts and other aerodynamic objects. In aerodynamics, pressure taps are used to measure the pressure distribution on the surface of an object, which provides valuable information for understanding the flow patterns and aerodynamic performance of the object. This information is crucial for aerodynamicists and engineers to design, analyze, and optimize the performance of aircraft and other aerodynamic objects.

The use of pressure taps in aerodynamics has a long history, dating back to the early days of aviation. Over time, pressure tap technology has evolved and improved, with the introduction of new materials, manufacturing techniques, and measurement methods. Today, pressure tap technology is a sophisticated field, with a wide range of different types of pressure taps available to meet the specific needs of aerodynamic testing. The first investigation of rapid prototyping used to create solid models for wind tunnel testing dates

back to 1998 by Springer [2]. The study involved the production of several models using both rapid prototyping methods and traditional manufacturing methods. The aerodynamic characteristics of these models were then tested in a wind tunnel and compared. The results of the study showed that the models produced using rapid prototyping methods had comparable aerodynamic characteristics to those produced using traditional methods. The authors also discussed the potential benefits of using rapid prototyping methods in wind-tunnel testing, such as reduced lead time and cost, improved design freedom, and the ability to quickly produce multiple iterations of a design [3]. The capacity to manufacture internal features that would be challenging to execute using traditional procedures is one of the most useful aspects of the additive manufacturing-based process [3, 4, 5, 6, 7, 8, 9].

Hynes explains how rapid prototyping technology has evolved in recent years and how two specific methods, Filament Deposition Machines (FDMs) and Stereolithography Machines (SLAs), are suitable for wind-tunnel-model production [3]. The article highlights the advantages of using rapid prototyping techniques over traditional methods, including the ability to incorporate internal features, weight savings, and faster time from CAD model to production. The article concludes with two case studies, showing how rapid prototyping techniques have been used to produce wind-tunnel models. A small model with a chord of 70 mm and a half-span of 220 mm was used to measure the spanwise wing-load distribution in the surface-pressure model case study that was reported in the article. 416 pressure tapping points were placed at 16 spanwise and 13 chordwise places on the upper and lower surfaces of the wing to create the three-dimensional CAD model [3]. To increase the speed of manufacture, the model was split into five sections and made using an SLA machine, with a manufacturing time of approximately 8 hours. The post-processing steps included

washing the parts in solvent to remove excess resin, post-curing in a UV chamber for 2 hours, and final assembly using an epoxy resin adhesive. A 0.35-mm drill was used to clean out the surface-pressure holes, and tubes were added to the wing-mounting end for connection to a manometer. According to the study, this way of manufacturing is still quicker and more effective than conventional ones, including inserting the spanwise tubes into slots cut into the wing surface.

2.3. Applications of RP-based models

2.3.1 Models for subsonic/transonic tests

Selective Laser Sintering (SLS) was used to create a wind tunnel model with a lambda wing-body configuration [10, 4, 5]. They started with the outside surface and designed the internals, including static pressure taps and the wind tunnel balance, before making the model. However, they were not able to measure the pressure as the taps had internal cracks and damages. Meanwhile, an Iranian joint group evaluated the feasibility of various Additive Manufacturing (AM) processes for model fabrication, such as SLS, Fused Deposition Modeling (FDM), 3D printing, Stereolithography (SL) etc. FDM was employed to show off its capacity to produce wind tunnel model parts in a fast and economical manner [6]. Due of their lower cost and quicker construction, 3D-printed models are suitable for initial testing. These printers were utilized by Bykerk from the University of Sydney to create hypersonic aircraft models for testing in a low-speed wind tunnel [8].

2.3.2 Models for surface-pressure measurements

The goal of wind tunnel testing for surface pressure measurements is to get preliminary data on the distribution of aerodynamic load. This information is used to

evaluate the aerodynamic performance and flow characteristics of the aircraft and its components. Monitoring the location of the minimum pressure locations on the wing, airflow separation patterns, lift, differential pressures, and the pressure center can help researchers gain a better understanding of these factors. The pressure measurement model has pressure holes running along the surface's normal direction, which are linked to measuring instruments such as pressure gauges or sensors through tubes. Zhou et al. studied the impact of defects such as hole shape, axis inclination, near-hole protrusion/depression, and scratches on pressure measurement [9].

3D printing is well-suited for the production of 3D printed wind tunnel models as, whose accurate results have proven reliable [11]. Additionally, Heyes and Smith at Imperial College London created a surface-pressure model with SL using pressure taps with a 0.35 mm diameter and a 70 mm chord [3]. Those taps were drilled and were further printed in various sections at the point it could be manufactured with traditional techniques better. The model had a span of 6 inches however they divided the print into 5 sections. Furthermore, Moioli investigated the quality of the model finishing, stiffness, and geometric accuracy to determine if the manufacturing technique can produce a suitable test device [12]. The pressure taps for steady surface pressure readings were included into the 3D printing process, and the study concentrated on the manufacture of complicated three-dimensional highly swept wings, with computational fluid dynamics techniques used to validate the experimental results [12]. Similarly, Gatto [13]worked on measuring the mean and fluctuating pressures on the surface of a traditionally manufactured circular cylinder subject to a cross-flowing airstream.

2.4 Applications of 3D Printed Pressure Taps in Vortical Flows

Engineers actively seek to manipulate flows to maximize benefits. The precise features of the involved flows, as well as the lift force produced over aircraft wings, have a significant impact on performance. Due to its efficiency, simplicity, low production and installation costs, and passive flow control effectiveness, vortex generators (VGs) are a common technique. Because the fluid must move around this obstruction, a vortex forms near the surface. Their basic working principle is that they produce stream wise vortices that energize the local boundary layer (BL), which brings high momentum fluid from the free stream closer to the solid surface and delays separation.

Vortex generators, as shown in Figure 2-1, are passive flow control devices attached to a surface that provide an accelerating force in the crossflow direction. A low-pressure zone known as the suction side is formed at the back side of the VG. Because of pressure difference between the front and back sides, VG generates a tip vortex that follows it downstream.

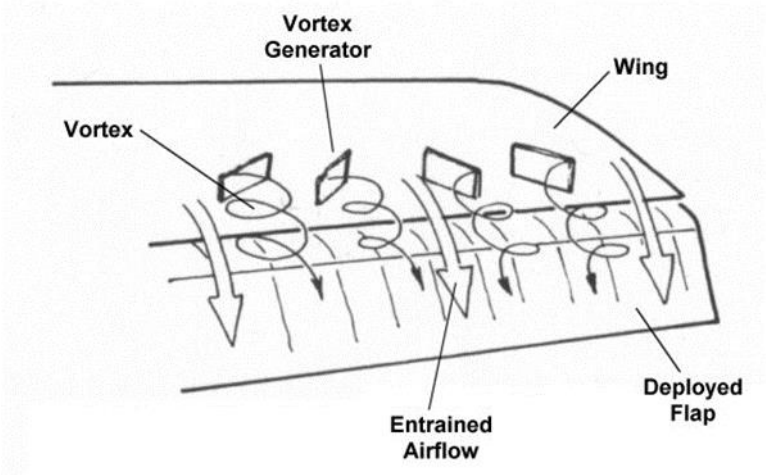

Figure 2-1: Vortex generator on an airplane wing.

There have been numerous studies done on the intricate features of the vortex formations that form as a result of the flow around a VG and how they interact with the boundary layer, including [14, 15, 16, 17, 18]. Furthermore, VG's has also been applied not only to aerodynamics but also have been used in bi-leaflet mechanical heart valve designs against blood damage and platelet activation [19]. The advantageous flow-mixing properties of the VGs have a drag penalty as a trade-off. The VG surface's skin friction and its induced drag contribute to some of this, but the form drag caused by the divided flow zone on the VG suction side accounts for the majority of the cause [17]. Reducing the size of the VG, especially its height, is one way to lower the drag penalty [20]. A more recent design known as submerged VGs has a height that is only one-third or less of, whereas standard VGs have a height that is roughly equivalent to the boundary layer's thickness. The amount of parasitic drag is significantly decreased as a result of this size reduction. Moreover, it has been discovered that the tip vortex that forms over a submerged VG has the capacity to expand until it almost entirely encloses the apparatus vertically, restricting flow separation over the VG's suction side and favorably impacting the amount of form drag [21]. Research from the past few decades has demonstrated that submerged VGs can delay flow separation just as well as conventional VGs [20].

VGs can be categorized into two main types, counter-rotating configuration and the parallel co-rotating configuration, as shown in Figure 2-2. Further classification of the counter-rotating configuration can be made based on the orientation of the VGs. The geometry and position of the VGs play a crucial role in determining the created vortex structures under a given flow situation. The arrangement of VGs within the array is critical as it can significantly affect the downstream development of streamwise vortices due to

interaction effects. However, designing an optimal VG array is a complex task, as the geometry, positioning, and flow conditions are strongly interdependent.

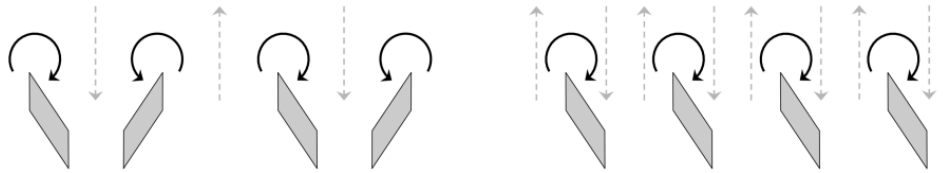

Figure 2-2: Counter-rotating and Co-rotating VG array.

A triangular VG is preferable than a rectangular VG since the drag penalty is reduced due to the smaller planform area. The effectiveness of triangular vanes is higher than that of rectangular ones. Several factors can parameterize the vortex generator geometry based on its angle, height and distance.

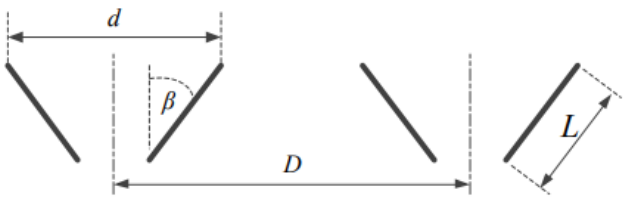

Figure 2-3: Arrangement parameters for vortex generator pairs.

The use of 3D printing technology has opened up a new realm of possibilities for investigating the effectiveness of vortical flows in aerodynamic applications. Specifically, the integration of 3D printed pressure taps presents a unique opportunity for measuring pressure on a 3D printed airfoil with vortex generators. Such a configuration presents a challenging flow condition that demands accurate and reliable measurement techniques. By accurately measuring the surface pressure, valuable insights can be gained into the performance of the vortex generators and the resulting flow control. However, the

effectiveness of the designed 3D printed pressure taps in capturing pressure measurements in vortical flows must be evaluated in order to ensure the validity and reliability of the data obtained. This is especially important given the complexity of the flow conditions involved. Thus, the evaluation of the effectiveness of the 3D printed pressure taps in measuring pressure in such complex flows is crucial in determining their potential for future use in a wide range of aerodynamic applications. Additionally, changes in the pressure coefficient between the airfoil with vortex generators and the airfoil without vortex generators will be analyzed to determine the effectiveness of the vortex generators in controlling flow separation. This analysis will provide important information about the flow behavior over the airfoil with vortex generators and will help to identify any areas for potential improvement or optimization. Overall, the integration of 3D printed pressure taps into the study of vortical flows has the potential to greatly enhance our understanding of aerodynamic systems and to pave the way for the development of more efficient and effective designs in the future.

CHAPTER 3. EXPERIMENTAL METHODOLOGY

Chapter 3 presents the experimental methodology used to explore the aerodynamic performance of a cylinder and a NACA 2412 airfoil with and without vortex generators. The chapter commences by outlining the design and manufacturing process of the 3D printed prototypes, emphasizing the meticulous consideration that was given to the incorporation of pressure taps for accurate measurement of the pressure distribution. Moreover, the chapter elaborates on the design and application of vortex generators on the airfoil, highlighting the essential parameters that were taken into account during their development. In addition, the chapter details the wind tunnel facility and instrumentation employed to gather data during the experiments.

3.1 Why SLA?

There are several types of 3D printers, each with its own strengths and limitations. The most common type of 3D printer is FDM, which works by melting a filament of thermoplastic material and extruding it through a nozzle. This process is relatively simple and affordable, making it a popular choice for hobbyists, small businesses, and educational settings. FDM printers are also able to print with a wide range of materials, including PLA, ABS, PETG, nylon, and more. Another type of 3D printer is SLA, which uses a light-reactive thermoset materials called “resin” resin that is cured by ultraviolet light. This process involves using a ultraviolet light to selectively cure the resin layer by layer, creating a three-dimensional object, as shown in Figure 3-1. SLA printing was first developed in the 1980s, and it has since become a popular and widely used 3D printing technology [22].

Figure 3-1: Schematic diagram of SLA printer [22].

SLA 3D printing is becoming increasingly popular among engineers, designers, manufacturers, and other professionals due to its ability to produce highly accurate and precise models with exceptional surface finish. One of the most significant advantages of SLA printing is its isotropic nature, which means that the mechanical properties of the parts produced are consistent in all directions. SLA printing produces parts with consistent qualities in all directions, in contrast to extrusion-based printing technologies like FDM, which are renowned for being anisotropic and produce parts with differences in strength depending on the orientation of the part relative to the printing process.

This isotropy is achieved through a combination of factors that are tightly controlled through the integration of material chemistry with the printing process. The resin components create covalent connections while printing, but the part is still in a partially reacted "green state" while it is built up layer by layer [22]. The polymerizable groups in the resin retain the ability to form bonds across layers during the final curing process, which imparts isotropy and watertightness to the part. The resulting parts have predictable mechanical performance since there is no variation in the molecular structure across the X, Y, or Z planes. This makes them perfect for applications like jigs and fixtures, end-use

parts, and functional prototypes. By depositing lines of PLA or ABS, FDM 3D printers build up layers. Layers may not entirely adhere to one another as a result of the process, which results in voids between the rounded lines and a weaker link between layers than the lines themselves (filament extrusion).

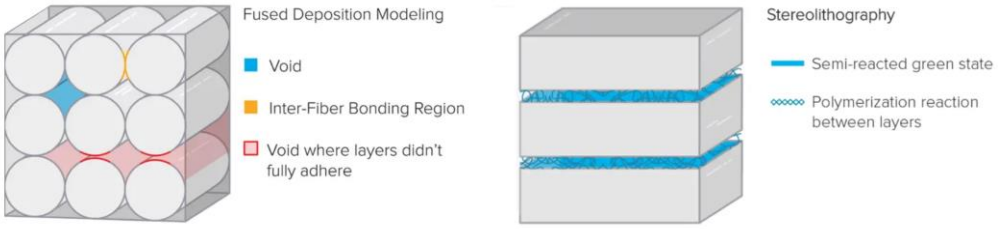

Figure 3-2: Isotropic nature of SLA prints [22].

Another advantage of SLA printing is its ability to create watertight geometries, Because of the highly accurate layer-by-layer printing process, SLA prints are fully solid and free from porosity, ensuring that the geometry is water or air-tight. This property is essential for applications that require a high level of precision, such as medical implants, aerospace parts, and electronics enclosures.

Moreover, SLA printing allows for even greater control over the accuracy of the final product. Pressure taps are small holes or channels that can be built into the part during the printing process, which allows for the precise pressure measurements at different points in the part. This level of control over the final product is critical for applications that require precise and consistent results, such as fluid dynamics research, microfluidics, and other scientific applications.

The ANYCUBIC Photon Mono X 6K used in this research is a top-of-the-line SLA 3D printer that offers exceptional print quality and precision. It features a large build

volume of 245 x 197 x 122mm, allowing for the printing of larger and more complex models. The printer also utilizes a monochrome LCD screen with a 6K resolution, which increases the light intensity and shortens the exposure time, resulting in faster print speeds and higher accuracy. Additionally, the Mono X 6K is equipped with a matrix UV light source that provides even and consistent UV light distribution throughout the build platform, ensuring that each layer is cured uniformly. The printer also comes with a user-friendly interface that allows for easy operation and intuitive navigation of the printing process as shown in Figure 3-3.

Figure 3-3: ANYCUBIC Photon Mono X 6K SLA printer.

Table 1 presents the specifications for the SLA printer.

Table 1: Photon Mono X 6k specifications.

Photon Mono X 6K	
Machine Size	475x290x270mm
LCD Resolution	5760x3600px (6k)
LCD Size	9.25" monochrome
XY Resolution	34 microns
Z axis Accuracy	10 microns
Build Volume	245x197x122mm
Max. Printing Speed	80mm/h

3.2 3D Printed Airfoil

The National Advisory Committee for Aeronautics (NACA) created the NACA 2412 airfoil, a popular aerodynamic profile, in the early 1920s. It is a non-symmetrical airfoil with a maximum thickness of 12% of the chord length and a maximum camber of 2.5% of the chord length. The airfoil has a flat bottom and a rounded leading edge, with a sharp trailing edge. The NACA 2412 airfoil is commonly used in low-speed applications, such as general aviation aircraft, wind turbines, and model aircraft. It provides a good balance between lift and drag, making it an efficient choice for these applications. The NACA 2412 airfoil has been extensively studied and is well understood, making it an ideal choice for aerodynamic experiments and research. The profile coordinates of the NACA 2412 design are imported from XFOIL [23]. Figure 3-4 shows the profile shape.

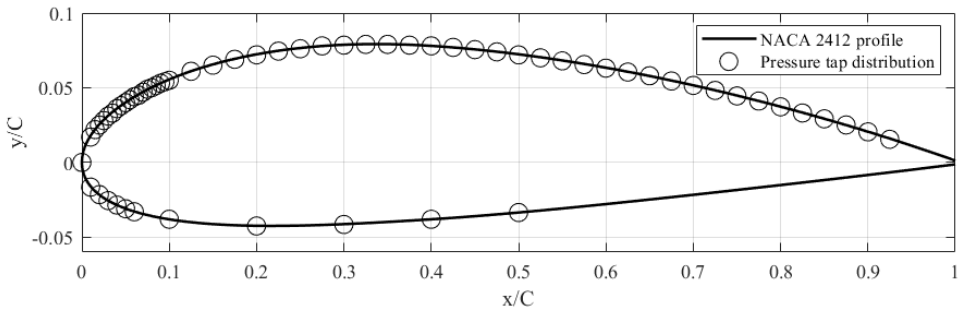

Figure 3-4: NACA 2412 airfoil and pressure taps locations.

XFOIL offers several capabilities that make it a valuable tool for airfoil design and analysis. One of its primary features is the ability to calculate the pressure coefficient distribution along the airfoil surface, which is a key indicator of the airfoil's performance. The pressure coefficient distribution shows how the pressure varies along the airfoil surface, providing insights into the lift and drag characteristics of the airfoil. In this study, the coordinates generated from the airfoil were imported into SolidWorks and a 3D sketch was made. The 3D model was constructed with a chord length of 9 inches (22.86 cm) and span of 7 inches (17.78 cm) as shown in Figure 3-5.

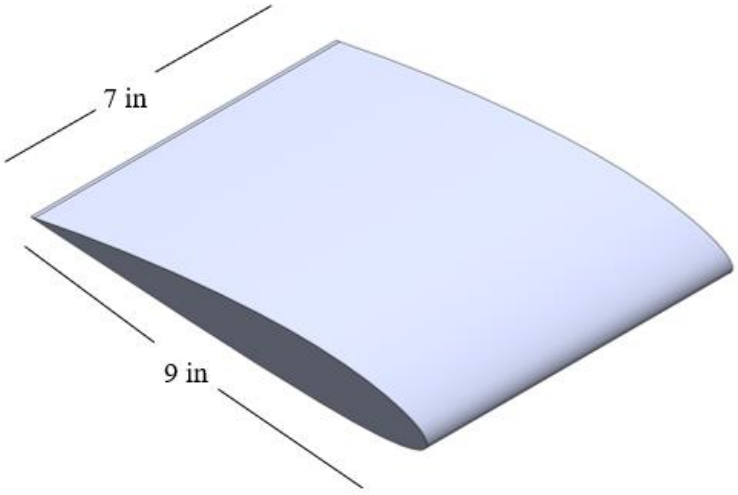

Figure 3-5: 3D model of NACA 2412.

3.2.1 Integrated Pressure Taps

The design of the pressure taps involved careful consideration of various factors to ensure that they would effectively measure the overall pressure around the airfoil. In total, 64 pressure taps were designed to be distributed along the surface of the 3D model of the airfoil created in SolidWorks. Overall location of the pressure taps are shown in Figure 3-4 and are tabulated for reference in Table A of Appendix A. The number of pressure taps was determined based on the capacity of the available pressure scanner for pressure measurements, which could measure up to 16 pressures at a time. The taps were arranged in three different configurations to ensure that the holes would not interfere with the holes behind them, thereby ensuring accurate pressure measurements. Airfoils with different configuration of pressure taps locations are shown in Figure 3-6, Figure 3-7 and Figure 3-8.

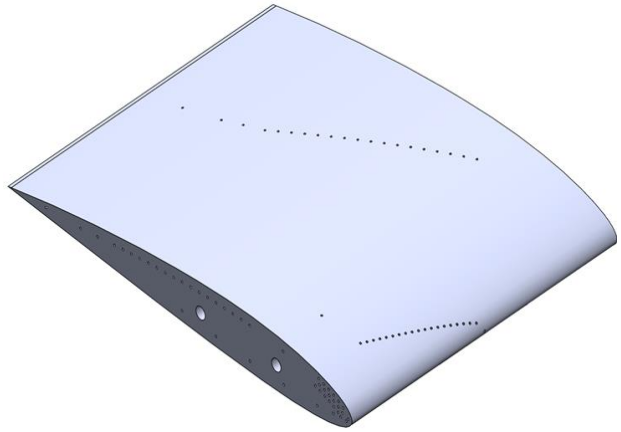

Figure 3-6: Pressure tap configuration 1.

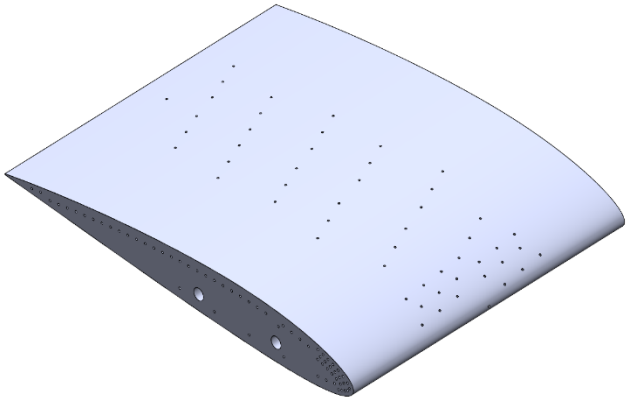

Figure 3-7: Pressure tap configuration 2.

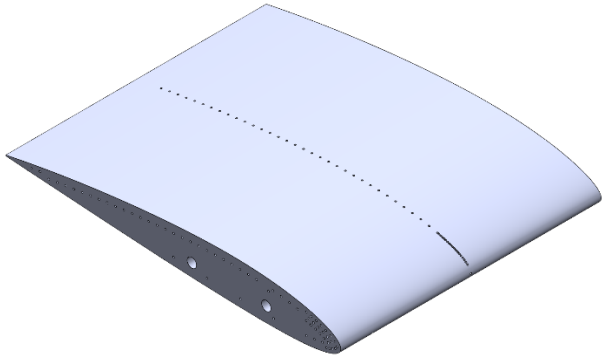

Figure 3-8: Pressure tap configuration 3.

In designing the pressure taps for measuring the pressure distribution around the 3D airfoil, a number of factors were taken into account. These included the size and shape of the airfoil, the desired accuracy of the pressure measurements, and the capacity of the pressure scanner. To ensure accuracy and precision, the taps were designed to be small enough to avoid interfering with the flow of air around the airfoil, while still large enough to effectively measure the pressure. Each pressure tap had a diameter of 0.042 inches (0.11 cm) and were carefully distributed to cover the entire surface of the airfoil, 45 taps on the upper surface and 19 taps on the bottom surface, enabling a comprehensive measurement of the pressure distribution. The upper surface of an airfoil typically experiences higher airflow speeds than the lower surface due to the curved shape of the airfoil. This means that there are more significant pressure variations on the upper surface, which requires more pressure taps to obtain an accurate pressure distribution measurement.

The taps were designed in SolidWorks by first sketching holes onto the airfoil surface, which were then extruded inside the surface and then on the spanwise row of the airfoil as shown in Figure 3-9. Each tapping was then fed into a hole size of 0.044 inches (0.11 cm) which were then connected to a stainless-steel tube, which in turn was connected

by a plastic tubing to the pressure scanner. Furthermore, two 0.25 inches (0.6 cm) holes were designed for a steel rod running through the mid-chord point.

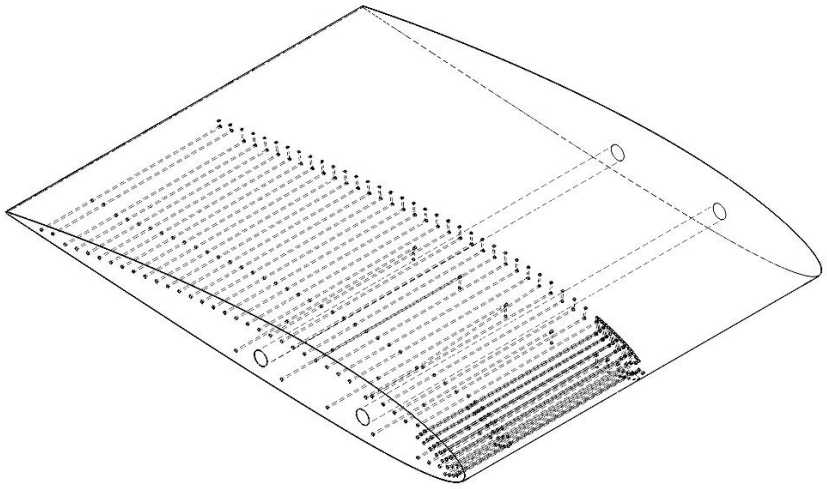

Figure 3-9: Pressure taps embedded into airfoil.

In contrast to the relative ease with which the pressure taps were designed and integrated into the airfoil in the current experiment, the manufacture of such intricate and small-scale features through traditional machining is far from straightforward. For instance, Fused Deposition Modeling (FDM) printers, which are commonly used for 3D printing, are typically limited in their ability to produce such fine and complex pressure lines with a high degree of accuracy and precision. This is due to the limitations inherent in the FDM process, which relies on the deposition of layers of material to create the final product. As a result, the level of detail and accuracy that can be achieved through FDM is often insufficient for applications that demand a high level of precision and intricacy, such as the design and manufacture of pressure taps for aerodynamic experiments. In light of these challenges, the successful design and implementation of the pressure taps in the

current study serves as a testament to the effectiveness of the design process and the expertise of the researchers involved.

3.2.2 Airfoil with Vortex Generators

The design of a vortex generator often involves several parameters that must be carefully chosen to achieve the desired aerodynamic performance. In this study, the boundary layer height was used as a parameter to determine the size of the vortex generator. The boundary layer height was first calculated through a 2D simulation of the flow past the airfoil at a post-stall angle of attack of 14º. The calculated boundary layer height was found to be approximately 4 mm, which was then used to determine the height of the vortex generator. As a result, a vortex generator with a height of 4 mm was considered for the setup. With the height of the vortex generator determined, further parameters were generated based on this value. These parameters included:

- Chordwise position of the VGs (x_{VG}/c): 0.3
- Height (h): 4mm
- Aspect ratio (AR) (h/L): 0.33
- Inclination angle (β): 15º
- Intra-and inter-spacing of VG vanes and pairs (d,D): (2h,7h)

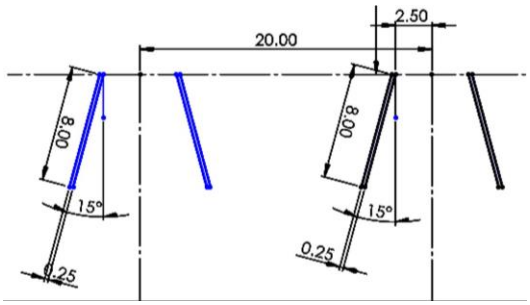

Figure 3-10: Vortex generators dimensions and arrangements.

After determining the sizing for the vortex generator, a 3D model was designed and assembled to the 3D airfoil model that included integrated pressure taps. To ensure accurate measurement of the VG effect, a few positions of the pressure taps were adjusted accordingly. The designed vortex generators were then printed using a FDM printer. The printer was configured precisely to print the VG with the required thickness, ensuring the accuracy and quality of the printed part. Once the print was done, the VG's were then glued to the surface of the airfoil.

3.3 3D Printed Cylinder

Flow over a cylinder is a well-studied problem in fluid mechanics due to its relevance in various industrial applications [24, 25, 26]. The flow characteristics over a cylinder can be complex, with the formation of vortices and turbulence, making it a challenging problem to study experimentally. 3D printing technology has made it possible to design and manufacture custom pressure taps that can be integrated onto a cylinder to measure the surface pressure distribution accurately. The design of these pressure taps is crucial in ensuring accurate pressure measurements in the presence of vortices and turbulence. The taps are typically designed to be flush-mounted with the surface of the

cylinder to minimize any disturbance to the flow. Additionally, the location and orientation of the taps are optimized to ensure that they capture the maximum pressure variation over the cylinder's surface.

In order to showcase the capabilities of 3D printing in designing pressure taps for pressure measurement on a cylinder, three different cylinder models were printed. The first cylinder model was designed with a straight pathway for the pressure taps, while the second cylinder model incorporated a more complex path with elbow bends, curved bends, and 45 degree bends. Third cylinder had a straight path but with smaller diameter. The complex path design was intended to demonstrate the advantage of 3D printing over traditional drilling methods, which would not be capable of producing such intricate designs. The sections below explain the design process for the pressure taps.

3.3.1 Straight Path Pressure Taps

Two different cylinders were designed for the straight path, with diameters of 3 inches and 0.4 inches. For the larger cylinder, 15 pressure taps were designed with 12-degree increments to cover the top half of the cylinder, while for the smaller cylinder, 9 pressure taps were designed with 10-degree increments. The design methodology for these pressure taps is similar to the steps described in Section 3.2.1 and is shown in Figure 3-11 and Figure 3-12. All of the pressure taps in this experiment have a diameter of 0.042 inches and were fed into a hole size of 0.044 inches (0.11 cm) each, which were then connected to a stainless-steel tube. The stainless-steel tubes were connected by plastic tubing to the pressure scanner.

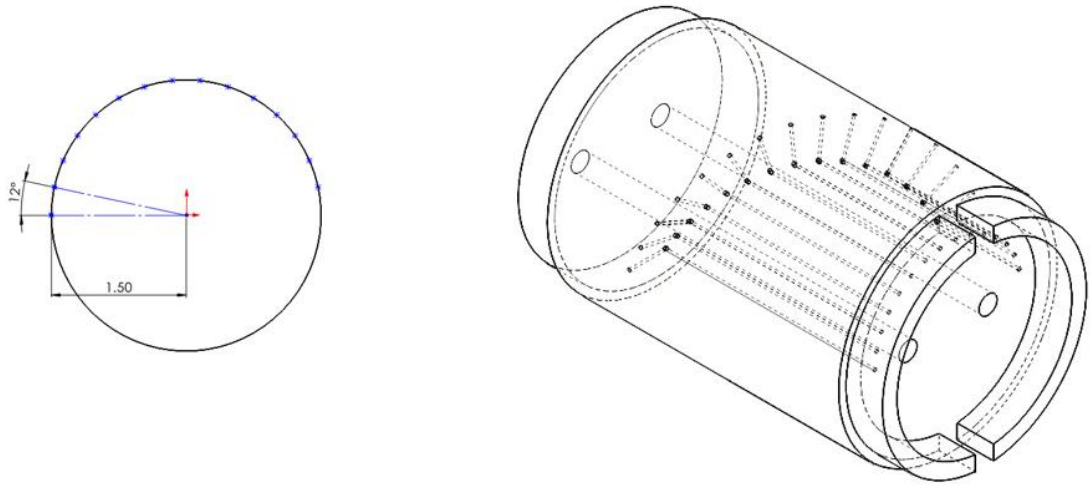

Figure 3-11: Cylinder with straight pathed pressure taps.

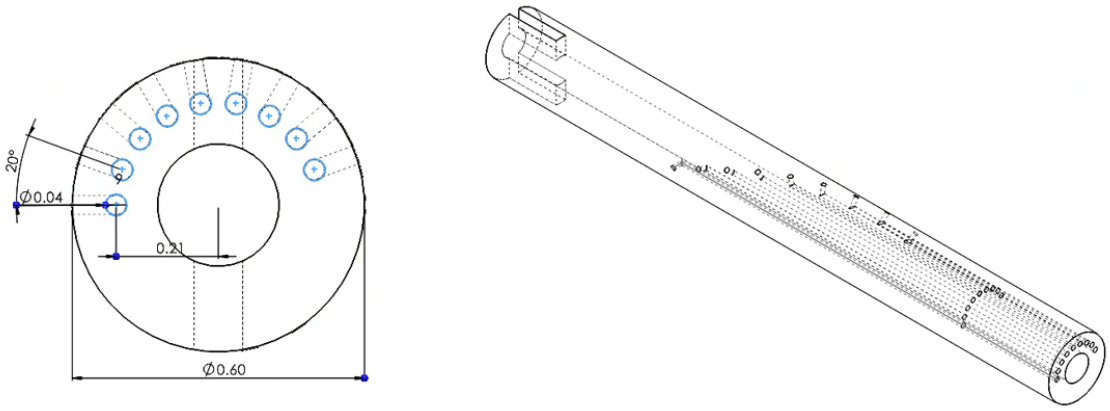

Figure 3-12: Small cylinder with straight pathed pressure taps.

3.3.2 Complex Path Pressure Taps

For the complex pathed cylinder, the design methodology was similar to the straight pathed cylinder, except that the path was designed to include a combination of elbow

bends, curved bends, and 45-degree bends. This design was meant to demonstrate the flexibility of 3D printing in creating complex geometries that cannot be achieved through traditional drilling methods. The complex pathed cylinder also had 15 pressure taps, with each tap placed at an increment of 12 degrees to cover the top half of the cylinder as shown in Figure 3-13. The diameter of each tap was 0.042 inches, and each tap was connected to a hole size of 0.044 inches (0.11 cm), which was then connected to a stainless-steel tube and plastic tubing to the pressure scanner. The pressure taps on the complex pathed cylinder were printed using the same SLA printer with a the same print resolution to that used for the straight pathed cylinder.

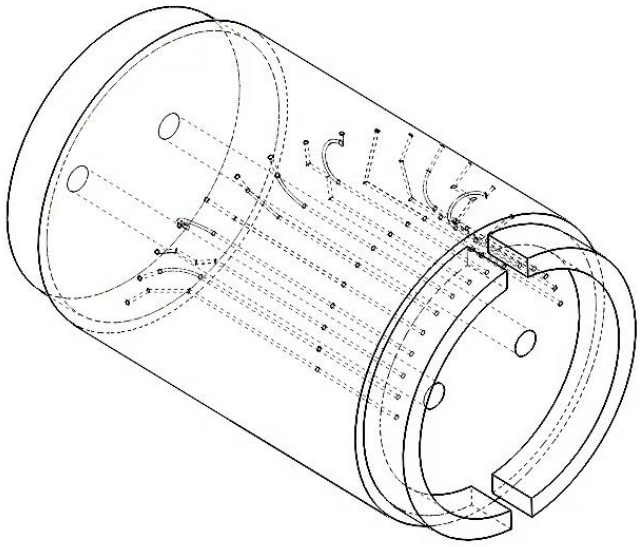

Figure 3-13: Cylinder with complex pathed pressure taps.

3.3.3 3D Printing: Process

The next step in the process was the conversion of the SolidWorks model into an STL file with the highest possible resolution. This file was then imported into Lychee Slicer, and the appropriate settings were applied as shown in Appendix. The resin used in

the printing process was a high-quality, UV-sensitive, water-soluble resin from ANYCUBIC. This resin was chosen for its high fluidity, fast curing time, and excellent stability in humid and corrosive environments. It also contains high-quality pigments, resulting in printed works with bright and vivid colors. To ensure optimal color distribution, the resin was thoroughly mixed before use. Additionally, the resin has a low shrinkage rate, which translates to high precision and a smooth surface finish in the printed model. The recommended storage temperature for the resin is between 15℃-35℃, and it should be stored in a sealed container to avoid exposure to moisture. Overall, the resin was selected for its suitability for use with DLP/LCD 3D printers, and its properties were found to be highly compatible with the printing process for the current project. Once the printing process was completed, the parts were washed with water to clean out the excess resin. To make sure that the resin inside the pressure taps were completely cleaned out, pressurized air was injected. Once the printed part look clean, it was then cured with UV light. Table 2 represents the print setup and process.

In addition to the SLA resin print of the cylinder and airfoil, FDM prints were also utilized for the side supports of the model. This was done in order to ensure that the flow would not be diverted sideways and to prevent any disturbances that may affect pressure measurement. The FDM prints were chosen specifically for this purpose, as they provided a strong and durable structure that could withstand the forces and vibrations of the wind tunnel test. The decision to use FDM prints only for the side supports and not for the pressure measurement components was made in order to maintain the highest level of accuracy and reliability in the pressure data obtained from the experiment. Furthermore, the holders for the test setup were also printed using FDM prints. Table 2 represents the

observations for the prints. FDM prints for the airfoil, cylinder and holders are as shown in Figure 3-14 and Figure 3-15.

Table 2: 3D prints evaluation.

	SLS	**FDM**
Color/Opacity	Blue (translucent)	Black, Orange
Surface roughness	Low	Moderate
Holes quality	All open	-
Print Time	8-14 hours	3 hours

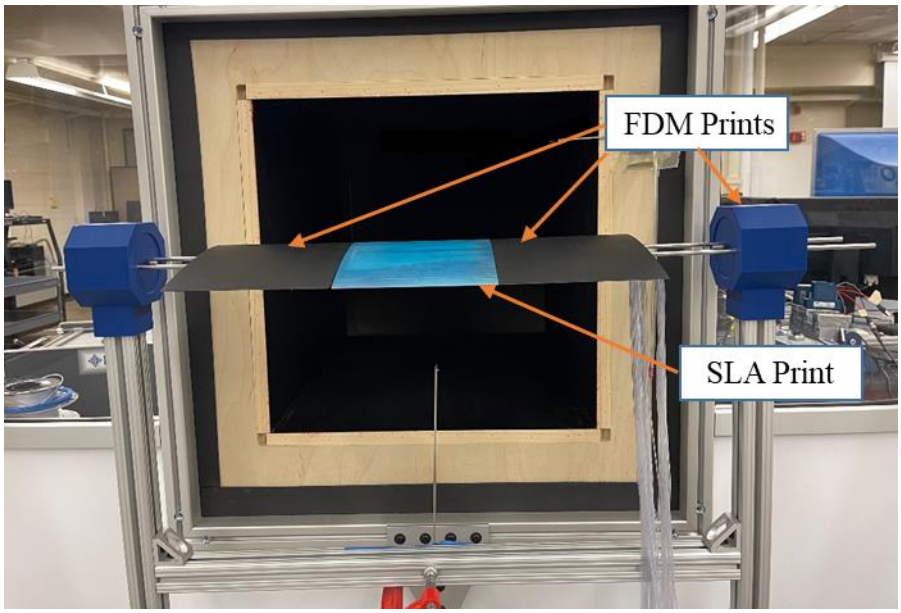

Figure 3-14: FDM prints of airfoils and holders.

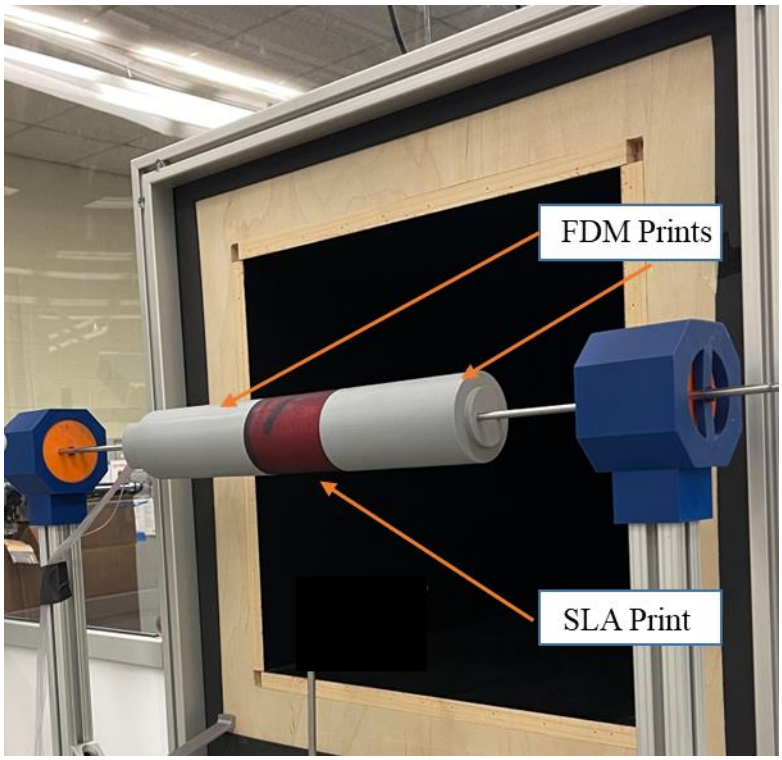

Figure 3-15: FDM prints for cylinders and holders.

3.4 Experimental Setup

Descriptions of the experimental setup are provided in this section. These include wind tunnel facilities, tests setup and instrumentation associated with data acquisition.

3.4.1 Closed Test Section Wind Tunnel

The 16” 16” subsonic wind tunnel at Youngstown State University (YSU) is a open loop wind tunnel as the working fluid passes through the test section and is not recirculated. The wind tunnel is divided into three sections: contraction, test section and diffuser. The wind tunnel works based on a rotating fan which sucks in the air and then passes through the outlet duct. Similarly, to control the velocity of the air, the wind tunnel is equipped with a rotating vane, which users can manually turn and control the flow rate inside the wind tunnel.

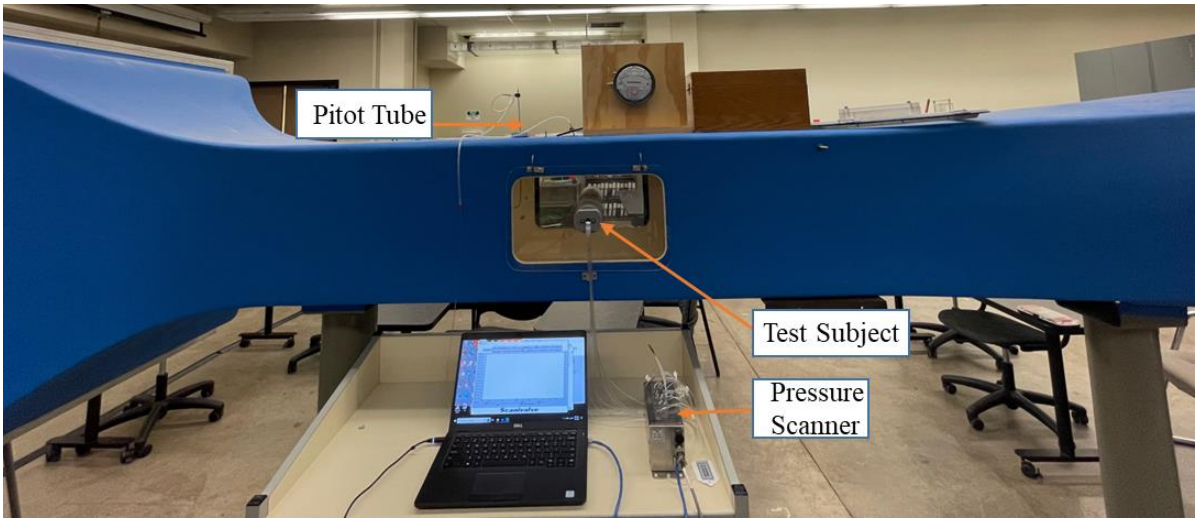

Figure 3-16: Subsonic wind tunnel at YSU

3.4.2 Open Test Section Wind Tunnel

The boundary-layer wind tunnel constructed in the YSU Fluid Dynamics Laboratory is an open-loop configuration using a diffuser, honeycomb, settling chamber, contraction, a flexible acrylic test-section ceiling for adjusting the pressure distribution, and a 40 hp blower motor as shown in Figure 3-17 and Figure 3-18.

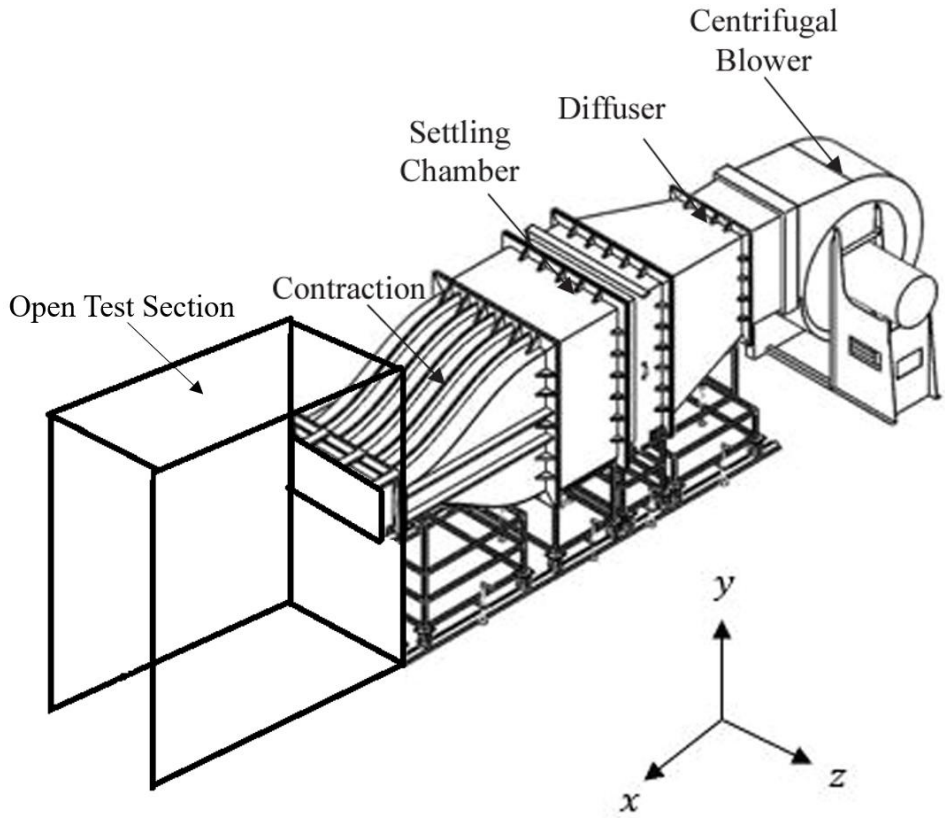

Figure 3-17: Schematic of open test section wind tunnel at YSU [7].

Figure 3-18: Open test section wind tunnel at YSU.

Blanco [7] predicted that the tunnel configuration paired with a 40 hp blower could surpass 30m/s. Power for the fluid's lab is isolated through an electrical disconnect box. Power is then provided to the inverter that serves as the variable frequency drive (VDF) for the blower. Once the main disconnect is switched on, power is passed to the inverter. The inverter panel displays the VFD frequency and other operational data. This panel has a reset button when the fault is tripped, commonly set off by adjusting the blower too quickly. The inverter panel was used to determine the frequency of the blower using the display screen values. The inverter panel is connected to a handheld controller that adjusts the blower motor frequency using a potentiometer.

To measure the wind speed an anemometer was used as shown in Figure 3-19. For the pressure measurements, the wind tunnel was ran at 10, 15 and 30 m/s. Figure 3-20 presents the test setup including the pressure scanner.

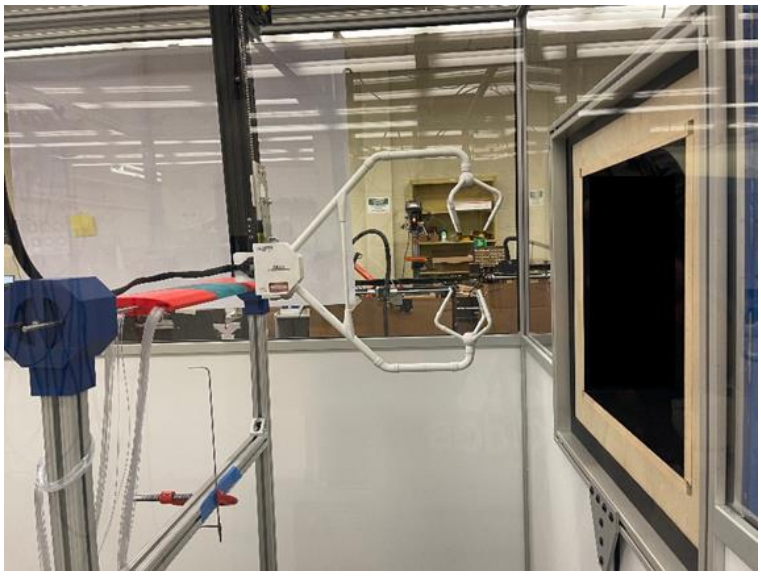

Figure 3-19: Anemometer for wind velocity measurements.

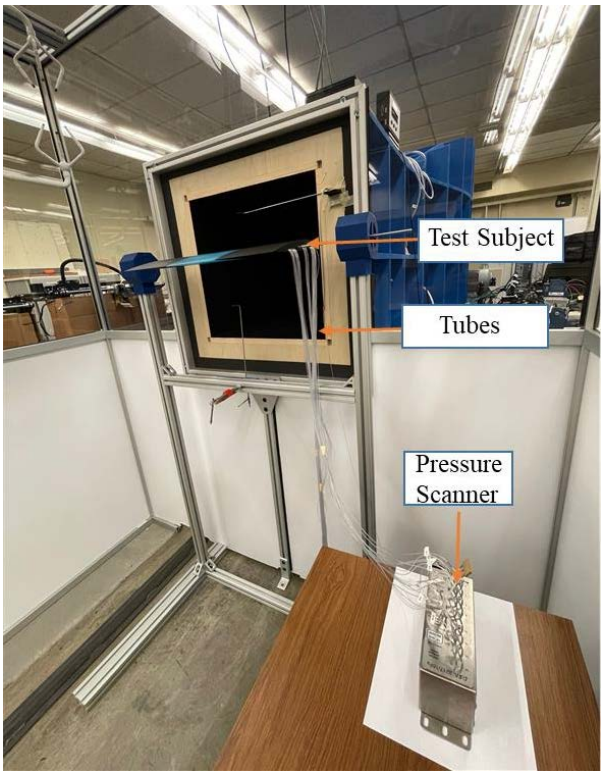

Figure 3-20: Test setup for open wind tunnel.

3.5 Data Acquisition and Uncertainty

The pressure measurement system employed in this study was the DSA3217-PTP pressure scanner. This module combines 16 temperature-compensated piezo resistive pressure transducers with a pneumatic calibration valve, RAM, 16-bit A/D converter, and a microprocessor. The scanner features an Ethernet interface for real-time data acquisition and transmission to a computer. The microprocessor compensates for temperature changes, converts units, and controls the actuation of an internal calibration valve for spontaneously zero and multipoint calibrations. The pressure acquisition system has a precision of ±0.2% of the full scale (±10 in. H2O).

The raw pressure data acquired by the scanner was processed using Scanivalve software, which provided pressure readings at each tap. The software also had the

capability to correct for temperature and sensitivity variations among the individual pressure sensors. The data was then exported to Microsoft Excel for further processing and analysis. The use of this advanced pressure scanner allowed for precise and accurate pressure measurements to be obtained, which were crucial for the analysis of the flow behavior around the cylinder and airfoil models.

The air density, velocity, and Reynolds number are computed using the stagnation pressure, room temperature, and barometric pressure. Throughout the testing cycle, the parameters are updated as the temperature and barometric pressure vary. Through the OMEGA temperature, humidity, and pressure recorder, these parameters are captured as shown in Figure 3-21.

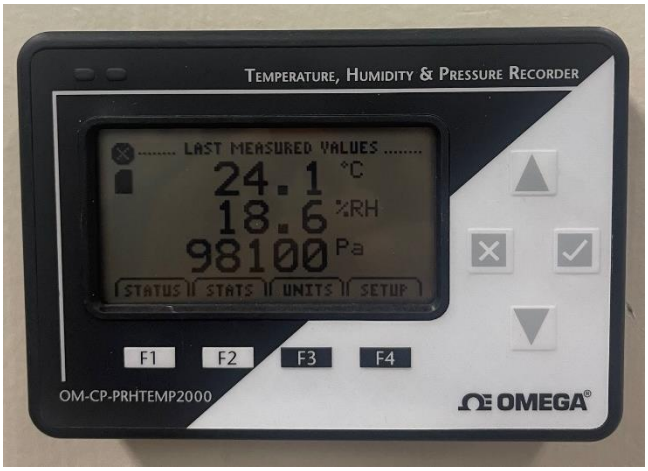

Figure 3-21: Temperature, humidity and pressure recorder.

Density of the air is calculated using the following equation:

$$\rho = \frac{P_{atm}}{RT} \quad 1$$

Where P_{atm} is the atmospheric pressure, R is the air gas constant and T is the room temperature.

Similarly, the velocity of the air was calculated as:

$$v = \sqrt{\frac{P - P_\infty}{\rho}} \quad (2)$$

Where P is the stagnation pressure and P_∞ is the freestream pressure.

Furthermore, Reynolds number was calculated as:

$$Re = \frac{\rho v L}{\mu} \quad (3)$$

Where L is the characteristic length and μ is the dynamic viscosity of air.

We then calculate the pressure coefficient based on following equation:

$$C_P = \frac{P_i}{P} \quad (4)$$

Where P_i is the pressure measured on each pitot taps.

Experimental error analysis is an essential aspect of scientific research that aims to establish the accuracy and reliability of experimental results. It involves identifying and quantifying uncertainties and errors associated with measurement techniques used to obtain data. These uncertainties can arise from factors such as measurement techniques, instrumentation error, data processing, and environmental factors. To establish accuracy and reliability of data, statistical techniques, calibration, proper experimental design, and procedures are used. Additionally, considering the resolution of the devices used in the experiment is important since it can impact the accuracy and precision of experimental measurements.

Since there are only ever going to be a finite number of measurements or data samples, statistical quantities that can approximate the statistical distribution of data from finite data sets must be constructed. For the experimental analysis, since multiple data sets

were collected for pressure measurements for each pressure taps, a standard deviation of the measurements was calculated, thereby a uncertainty analysis can be calculated as:

$$C_i = x \pm t_{v,P} S_x \quad (5)$$

Where $t_{v,P}$ is Student's t-distribution. For the uncertainty, the student's distribution is assumed at 95% confidence to establish an error band. For all the pressure measurements, 15000 samples were taken leading to a maximum standard error of 0.001097 psi for airfoil and 0.044305 psi for cylinder.

Furthermore, the measurements taken with the pressure scanner need to be analyzed. The pressure scanner has a precision of ±0.2% of the full scale (±10 in. H2O), which corresponds to 0.361 psi. Thereby, the error due to the scanner can be calculated as:

$$U_s = S_P S_{max} \quad (6)$$

Now, combining errors with standard pressure and device resolution via a root-sum-square gives the total uncertainty for the pressure measurements of 0.072 psi for airfoil and 0.084695 psi for cylinder.

3.6 Lift and Drag

Once the pressure coefficient was obtained, lift and drag for each position was calculated.

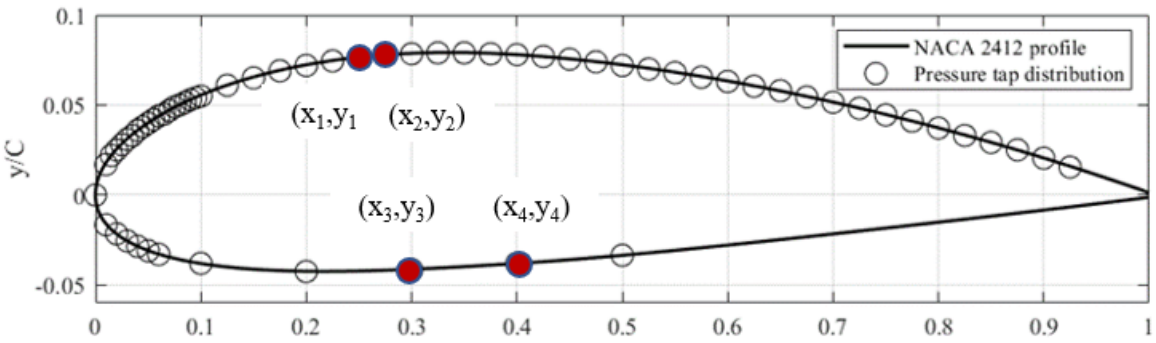

Figure 3-22: Coordinates for pressure taps.

Consider the pressure at each pressure taps at P_1, P_2, P_3, and P_4. Then, lift and drag for the upper surface is calculated as:

$$Lift[1,2] = -\frac{P_1 + P_2}{2}(x_2 - x_1) \quad (7)$$

$$Drag[1,2] = \frac{P_1 + P_2}{2}(y_2 - y_1) \quad (8)$$

Similarly, lift and drag for the lower surface is computed as:

$$Lift[3,4] = \frac{P_3 + P_4}{2}(x_4 - x_3) \quad (9)$$

$$Drag[3,4] = -\frac{P_3 + P_4}{2}(y_4 - y_3) \quad (10)$$

Now, the total lift and drag for the top and bottom surface can be calculated as following equations:

$$Lift[upper\ surface] = \sum_{1}^{n} -\frac{P_n + P_{n+1}}{2}(x_{n+1} - x_n) \quad (11)$$

$$Drag[upper\ surface] = \sum_{1}^{n} \frac{P_n + P_{n+1}}{2}(y_{n+1} - y_n) \quad (12)$$

$$Lift[lower\ surface] = \sum_{1}^{n} \frac{P_n + P_{n+1}}{2}(x_{n+1} - x_n) \quad (13)$$

$$Drag[lower\ surface] = \sum_{1}^{n} -\frac{P_n + P_{n+1}}{2}(y_{n+1} - y_n) \quad (14)$$

Then, the total lift and drag at an angle of attack can be found as:

$$L = Lift[total]cos\alpha - Drag[total]sin\alpha \quad (15)$$

$$D = Lift[total]sin\alpha + Drag[total]cos\alpha \quad (16)$$

Consequently, lift and drag coefficient can be calculated as:

$$C_L = \frac{L}{\frac{1}{2}\rho v^2 l} \quad (17)$$

$$C_D = \frac{D}{\frac{1}{2}\rho v^2 l} \quad (18)$$

CHAPTER 4. NUMERICAL SETUP

Chapter 4 of this study which is focused on computational fluid dynamics (CFD), begins with a discussion on the numerical setup, specifically the geometry and grid generation. The 2D domain was created using SolidWorks and exported as a STEP file for mesh generation in ANSYS ICEM mesh. The resulting mesh was verified for convergence through a comparison of the lift coefficient for the airfoil. Boundary conditions were assigned, with the airfoil and walls having a condition of no-slip wall and the inlets and outlets having specific conditions.

4.1 Geometry and Grid

The computational study was initiated by creating a 2D domain in SolidWorks, replicating the experimental setup for both wind tunnels, as illustrated in Figure 4-1 and Figure 4-2. Subsequently, the geometry was exported as a STEP file and imported for grid generation.

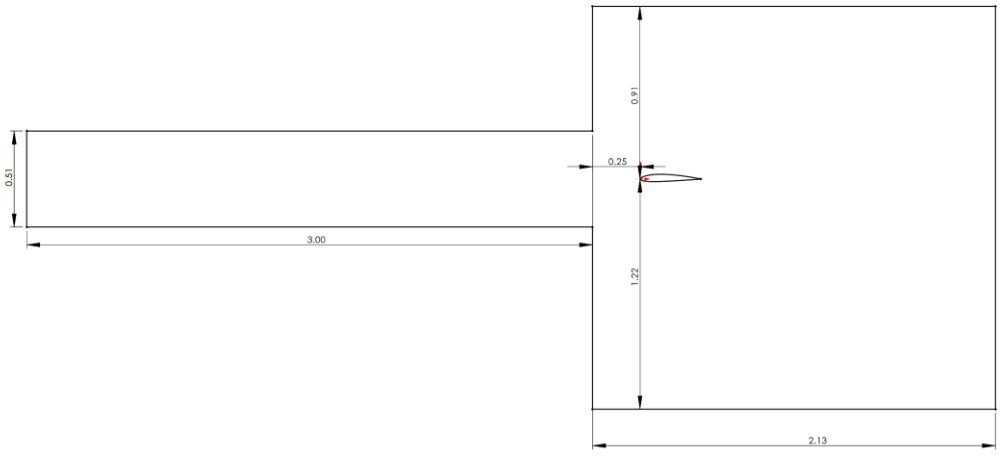

Figure 4-1: Computational domain for open test section.

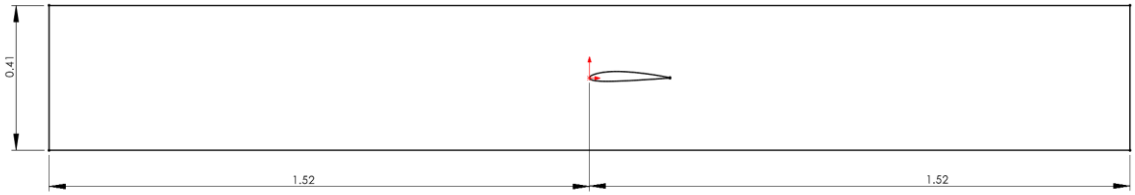

Figure 4-2: Computational domain for closed test section.

To ensure a successful solution through CFD, a suitable mesh was created using ANSYS ICEM mesh. Firstly, a block was established, and an O-grid was implemented. The blocks were subsequently divided into several smaller blocks to create a dense mesh region around the airfoil, as presented in Figure 4-3 and Figure 4-4. The number of edge spacings was allocated based on the requirements of dense elements near the airfoil and wall, and also to maintain the aspect ratio closer to 1. The spacing near the airfoil was inputted as 8e-5 m in a manner to achieve a y+ value of less than 1. Furthermore, a controlled spacing was applied towards the wall region of the domain to capture the boundary layer and establish a stable flow in the domain. In addition, both wind tunnel setups involved airfoils with a blunt trailing edge.

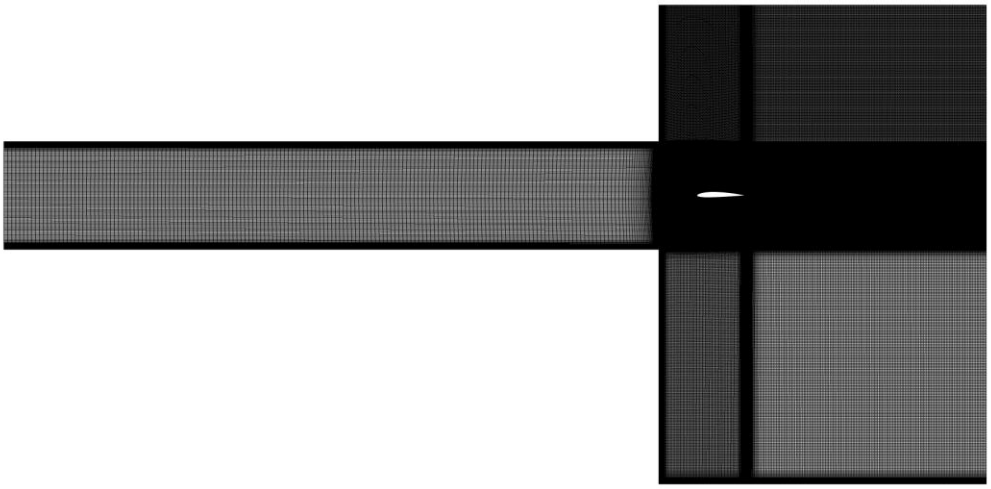

Figure 4-3: Full open test section mesh.

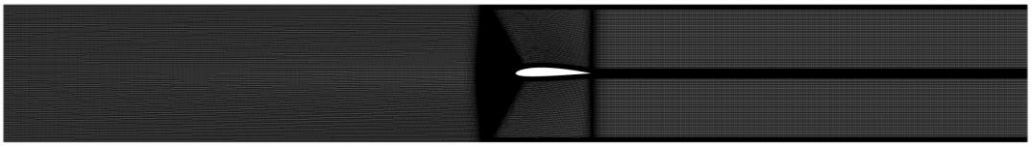

Figure 4-4: Full closed test section mesh.

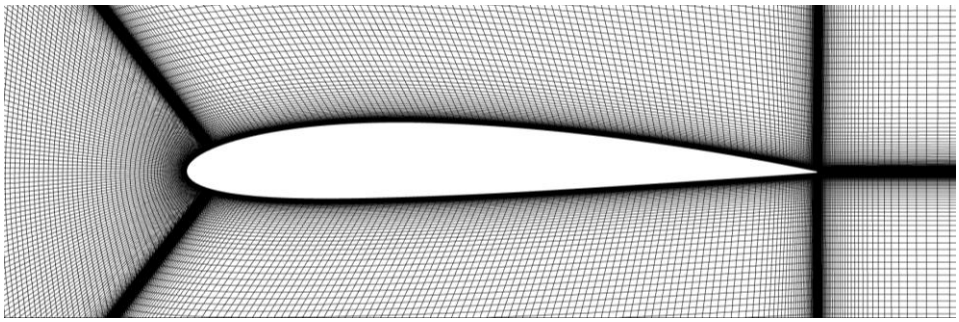

Figure 4-5: Mesh near airfoil.

Upon completion of the unstructured mesh generation, the resulting mesh was exported in a format readable by the ANSYS Fluent software package. The convergence of the mesh was subsequently verified through a comparison of the lift coefficient for the

airfoil. This analysis was conducted to ensure that a reduction in mesh elements would not significantly impact the lift coefficient. The mesh convergence results for both wind tunnels are presented in Table 3. The closed tunnel mesh exhibited a minimal change in Cl of only 0.2% with the reduction of mesh elements from 300k to 160k. Furthermore, a decrease in the number of elements to 70k resulted in a change in Cl of approximately 4.11%. Given these observations, a mesh containing 160k elements was selected for all subsequent simulations performed within the closed tunnel.

In addition to the element count and density, mesh quality parameters were also considered during the grid generation process. Mesh quality parameters ensure that the mesh is suitable for the CFD solution and provide an indication of the accuracy and reliability of the results. Several parameters, including minimum orthogonality, aspect ratio, cell quality, and skewness, were used to evaluate the quality of the generated meshes. The generated mesh had a minimum orthogonality of 0.45.

Table 3: Maximum percent difference in lift coefficient.

No. of Elements	**C_L**	**% Error**
70000	0.2012	4.11%
160000	0.20983	**-**
310000	0.2098	0.01%

4.2 Boundary Conditions

Initial and boundary conditions are assigned to the grids. For both model, airfoil and walls were assigned a condition of no-slip wall. Similarly, the outlets for the domain were assigned as pressure outlet while the inlet was assigned as an velocity inlet with a

magnitude of 15 m/s for open test section and 35 m/s for the closed test section as shown in Table 4 and Figure 4-6 and Figure 4-7. For the velocity inlet, turbulence specification method was selected for intensity and length scale. Turbulence intensity of 3% was applied with a length scale of 0.2 m. Similar turbulence parameters were also applied to the pressure outlet.

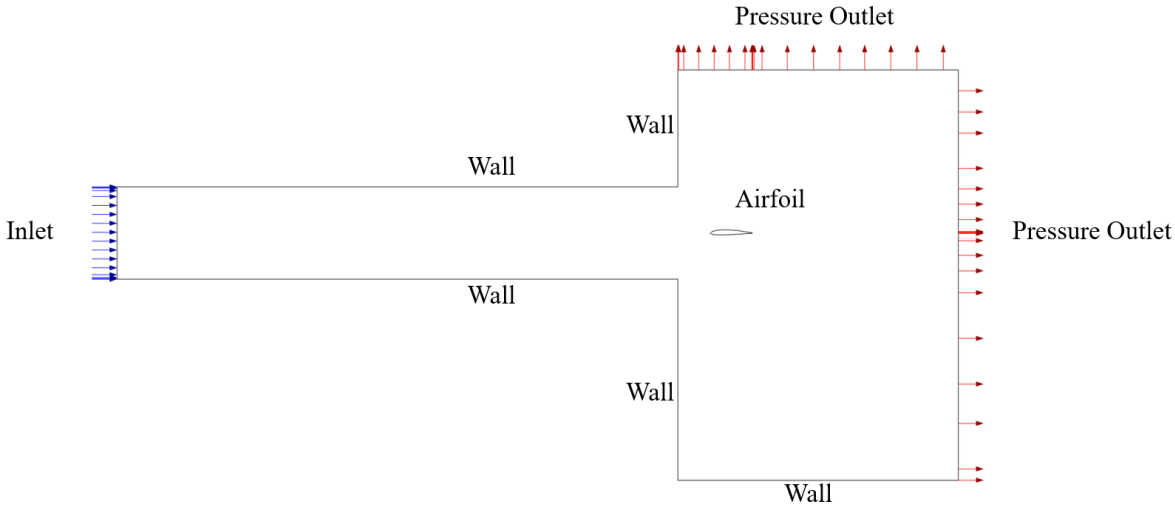

Figure 4-6: Boundary conditions for open test section domain.

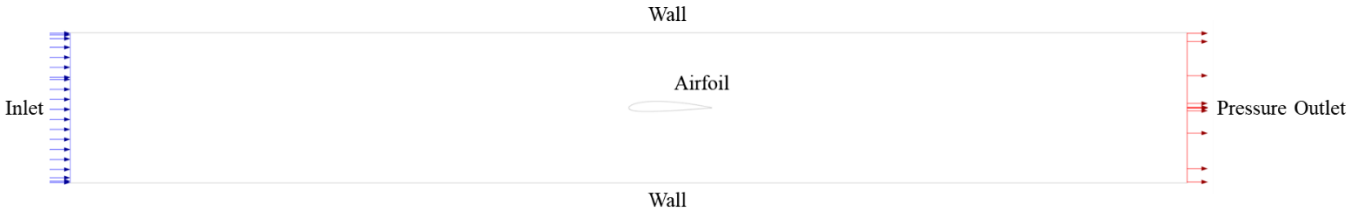

Figure 4-7: Boundary conditions for closed test section domain.

Table 4: Boundary conditions and its types.

Boundary Conditions	Type	Condition
Airfoil	Wall	No Slip
Wall	Wall	No Slip
Inlet	Velocity Inlet	Open Test: 15 m/s Closed Test: 35m/s
Outlet	Pressure Outlet	Gage Pressure = 0

Following the completion of meshing and application of boundary conditions, the mesh was subsequently exported to the computational fluid dynamics (CFD) software FLUENT for simulation. Recent studies on airfoil flow have demonstrated the effectiveness of various turbulence models, with Spalart-Allmaras and SST k-ω models being frequently cited in the literature [27]. In the present investigation, which involves steady-state Reynolds Averaged Navier-Stokes (RANS) simulations, the Spalart-Allmaras turbulence model was selected.

The Spalart-Allmaras turbulence model is a widely utilized one-equation model that has been extensively employed for airfoil simulations. This model is noted for its computational efficiency and simplicity and is especially suitable for modeling low Reynolds number flows. The SA model has proven capable of accurately predicting boundary layer development and separation on airfoil surfaces and is capable of capturing flow physics in the vicinity of airfoil leading edges.

4.3 Numerical Discretization

The ANSYS FLUENT software employs the Pressure-Based Solver algorithm for all computations, which is specifically designed for low-speed incompressible flows. To

obtain the velocity and pressure field, the method solves the momentum equations. The pressures are calculated using equation that is based on a combination of the continuity and momentum equations. Fluent offers several solver algorithms, including the segregated: SIMPLE, and PISO, and coupled algorithms. The segregated algorithm solves the governing equations one by one for each variable, which reduces memory requirements but slows down convergence. The SIMPLE (Semi-Implicit Method for Pressure-Linked Equations) algorithm uses a predictor-corrector method to achieve a faster convergence rate. The PISO (Pressure-Implicit with Splitting of Operators) algorithm also improves convergence by splitting the pressure correction equation into two steps but requires more computational time than the SIMPLE algorithm. The coupled algorithm solves the momentum equations and the pressure-based continuity equation as a coupled system. Coupled pressure-velocity coupling was selected. Second-order upwind equations were chosen for the spatial discretization of pressure, momentum and modified turbulent viscosity.

CHAPTER 5. RESULTS AND DISCUSSION

Chapter 5 presents the findings of the study, which aimed to investigate the flow behavior over 3D printed cylinders and airfoil with embedded pressure taps. The chapter begins by comparing the pressure coefficient plots for the straight and complex pathed pressure taps cases with the acrylic cylinder case. The chapter then discusses the validation of the experimental results with literature values. This section also presents the results and discussion of the performance of 3D printed pressure taps on the surface of a NACA 2412 airfoil which is divided into two subsections: closed test section data and open test section data. The study revealed that the pressure differences between the upper and lower surfaces of the airfoil increased with an increase in the angle of attack. Notably, the pressure coefficient on the upper surface was negative while that on the lower surface was positive, indicating the generation of lift on the wing. Moreover, the experimental findings exhibited a high degree of concurrence with the CFD simulation outcomes. Furthermore, the open test section data revealed the efficacy of the 3D printed pressure taps in capturing the complex flow features around the airfoil, including the effects of vortex generators installed on the airfoil.

5.1 3D Printed Cylinder Results

Comparing the data from the pressure coefficient plots for the three different cases, it is observed that there is a good agreement between the straight and complex 3D printed pressure taps path cases, while the acrylic cylinder machined pressure taps case shows some deviation as shown in Figure 5-1, Figure 5-2, and Figure 5-3. The pressure coefficients for the straight and complex cases are quite similar, with the differences in

magnitude of 8.54% being within the expected range of experimental error. On the other hand, the acrylic cylinder case shows some significant deviation from the other two cases, particularly at higher angles. This could be attributed to the difference in the geometry of the acrylic cylinder and the 3D printed cylinder, as well as the surface roughness of the 3D printed cylinders. Overall, all of the cylinders follow same pressure coefficient curve and depicts the same transition to separation at an angle of 70°.

The results of the comparison between the pressure coefficient plots for the straight and complex pressure taps path cases indicate good agreement, suggesting that the complex pressure taps path can serve as an alternative to the traditional straight pressure taps. However, there was a slight deviation observed among these cases, which could be attributed to surface roughness differences. Additionally, experimental errors, including slight variation in wind tunnel velocity and positioning of the cylinder, could also be a factor. Furthermore, the flow of air over the cylinder at the Reynolds number conducted generates vortical flows past the cylinder, leading to cylinder vibration and slight test section vibration. This may have caused some variation in pressure measurements between the two cylinders. Overall, these results for both cylinders are within the error bar and demonstrate the potential of 3D printing technology to produce complex shapes with embedded pressure taps for reliable flow measurement.

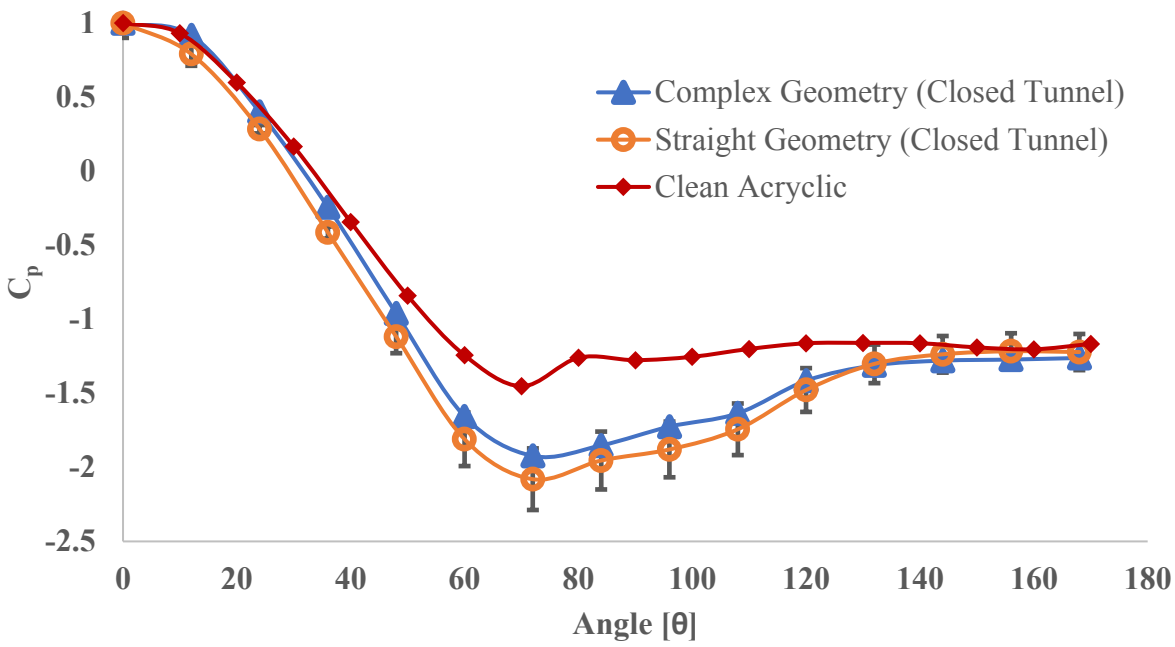

Figure 5-1: C_p comparison between 3D printed and acrylic cylinder for Re=1.54x10^5.

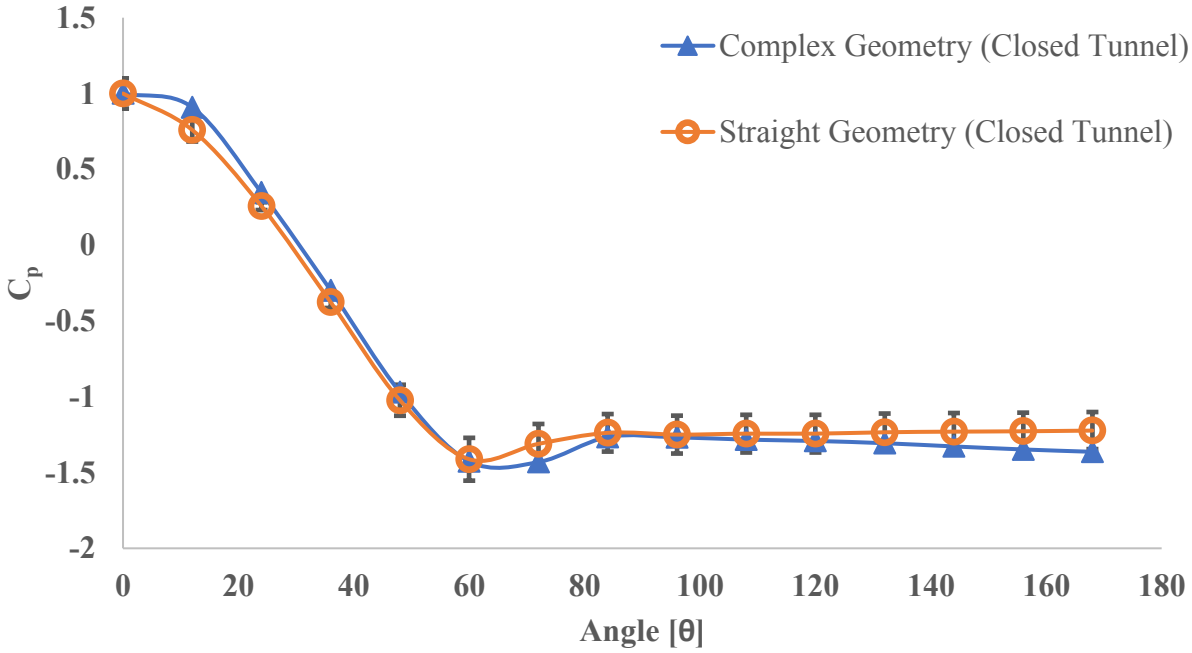

Figure 5-2: C_p vs. angle for Re=0.55x10^5 (Closed Tunnel).

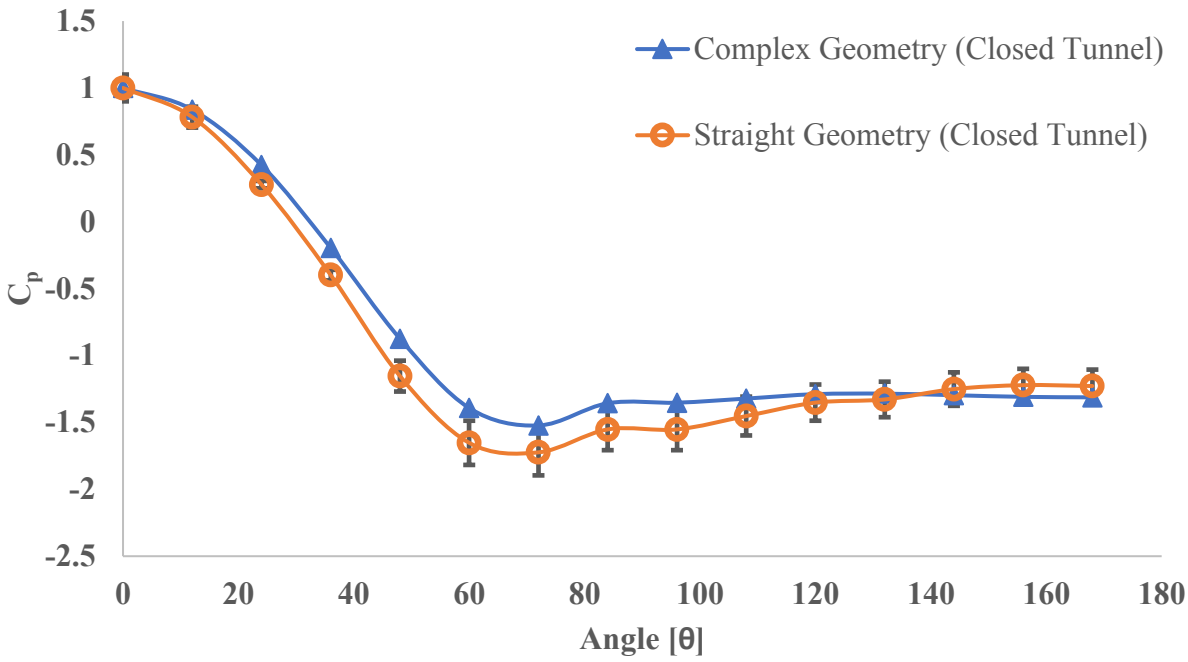

Figure 5-3: C_p vs. angle for Re=0.99x10^5 (Closed Tunnel).

The literature chosen for this study is the research paper by Young [25], which reports the Cp values for the flow over a circular cylinder at Re 4000 which closely match the values of experiment performed. The experimental data collected in this study were compared with the data presented in the literature to validate the accuracy of the 3D printed cylinder used in the current experiment as shown in Figure 5-4. The results of the comparison indicate that there is a close agreement between the experimental and literature values, with an average percent difference of 17.83%. This supports the conclusion that the 3D printed cylinder used in the experiment is a suitable model for investigating the flow over a circular cylinder. Moreover, the comparison of the experimental and literature data reveals that the flow over the cylinder exhibits the typical characteristics of the phenomenon, including a leading-edge separation and a gradual increase in Cp before the onset of a sharp drop associated with the onset of vortex shedding. The study concludes

that the experimental data obtained in this investigation can be relied upon for further analysis of the flow over a circular cylinder.

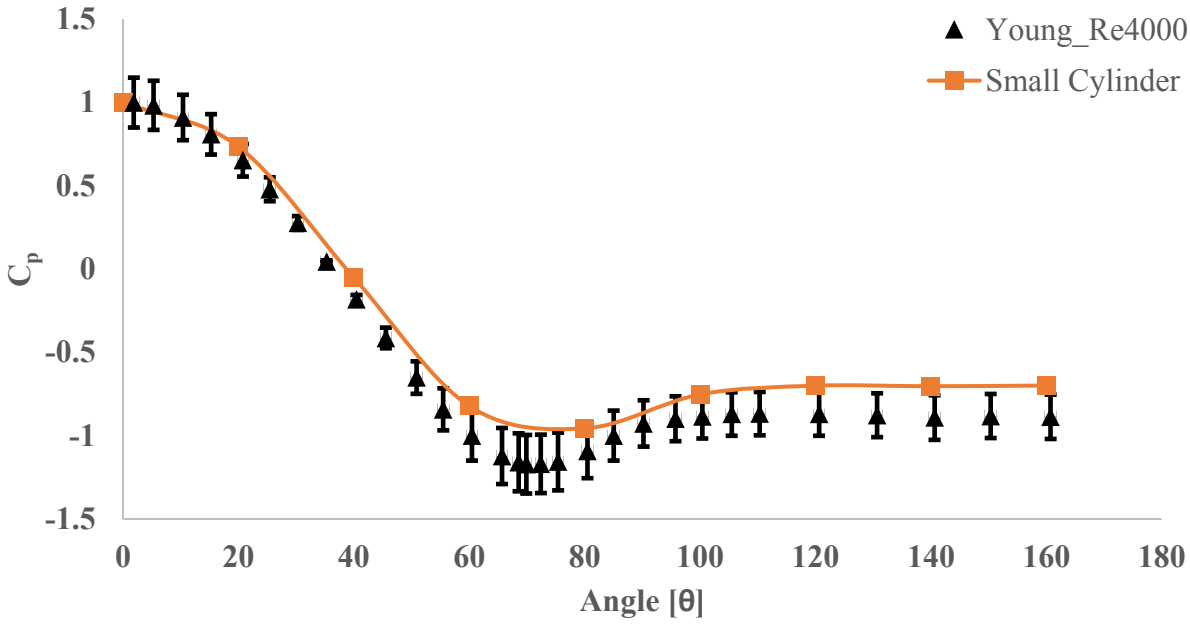

Figure 5-4: C_p validation plot for Re=4000.

In order to further validate the experimental results obtained at a different Reynolds number, another study conducted by Norberg [26] in 1987 was examined, which investigated the turbulence and Reynolds number effects on the flow and fluid forces on a single cylinder in cross-flow at a Reynolds number of 1.54e5. The data obtained from the study showed a similar trend to the experimental data obtained at the same Reynolds number. Both sets of data showed a sharp decrease in the coefficient of pressure as the angle of attack increased further from 0° to 90°. There was a slight difference in the magnitudes of the coefficient of pressure between the two sets of data as shown in Figure 5-5 . The data obtained from the study had higher magnitudes of the coefficient of pressure

compared to the experimental data. This difference in magnitudes could be attributed to the minor difference in experimental setup and positioning of the pressure taps. Furthermore, the difference in the pressure magnitude after separation can be accounted due to the surface roughness or even geometrical disparities between that of literature and experiment.

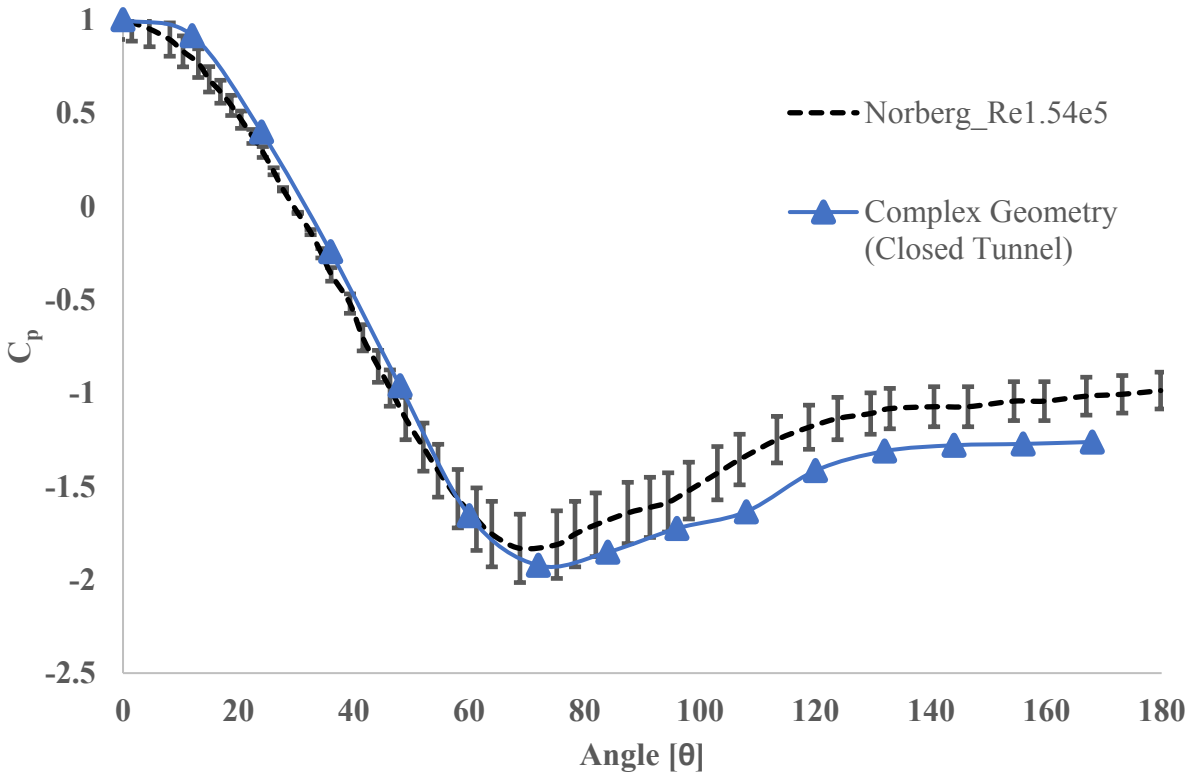

Figure 5-5: C_p validation plot for Re=1.54x10^5.

5.2 Cp Variation in Closed and Open Wind Tunnel

The difference in the Cp plot for the cylinder in the open test section wind tunnel as compared to the closed test section wind tunnel, as shown in Figure 5-6 could be attributed to several factors. One of the main factors is the difference in the boundary layer development over the cylinder in the two wind tunnels. In the closed test section, the

boundary layer over the cylinder develops under controlled conditions with minimal influence from the surrounding environment. On the other hand, in the open test section, the boundary layer over the cylinder develops in an uncontrolled environment, and the flow conditions are influenced by the surrounding atmosphere. The closed tunnel does not allow the flow to expand vertically as it passes over the cylinder. This results in local acceleration which reduces local pressure. In the open tunnel the flow is free to expand vertically as it passes over the cylinder and thus it does not accelerate and it does not drop in pressure.

Additionally, the presence of turbulence and vortices in the surrounding atmosphere in the open test section wind tunnel could also affect the flow behavior over the cylinder. The turbulence can cause the boundary layer to be thicker and more turbulent, which in turn can affect the separation and reattachment points on the cylinder surface. These changes in the separation and reattachment points can cause changes in the pressure distribution on the cylinder surface, resulting in a different Cp plot.

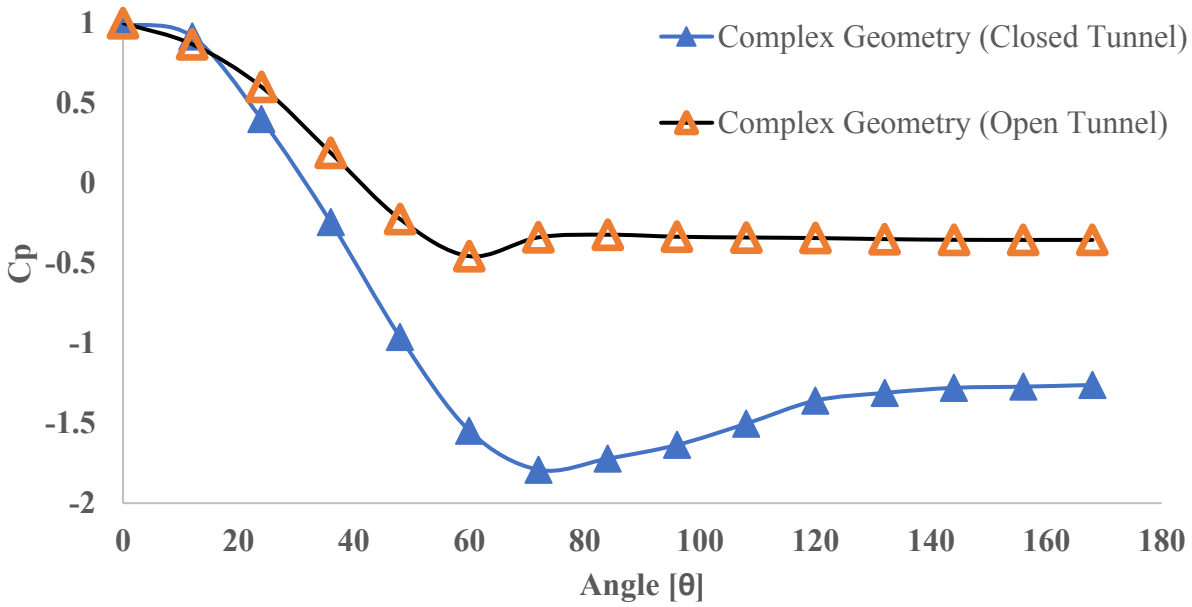

Figure 5-6: C_p comparison between open and closed wind tunnel.

Moreover, the difference in the reference pressure used in the pressure scanner for DAQ could also contribute to the difference in the Cp plot between the two wind tunnels. In the closed test section, the reference pressure is typically taken as the freestream pressure measured by the pitot tube. However, in the open test section, the reference pressure is often taken as atmospheric pressure. The difference in the reference pressure could lead to errors in the pressure measurements and, consequently, in the Cp plot.

5.3 3D Printed Airfoil Results

5.3.1 Closed Test Section Data

The pressure distribution of a NACA 2412 airfoil under various angles of attack (AoA) was investigated, and the results are presented in Figure 5-7, Figure 5-8, and Figure 5-9. For the experiment conducted in closed test section, the angle of attack for the airfoil was offset by 2°, thereby for measurements taken at 2° and 5° AoA, the experimental value

matched with 0° and 3° AoA from XFOIL and CFD. This method has been widely applied in various experimental works and the main reason behind this adjustment is the 3-dimensional effects created by the interaction of the boundary layer formed on all of the tunnel walls and the airfoil [28, 29]. The data shows that the pressure differences between the upper and lower surfaces of the airfoil increase with increasing AoA. The pressure differences at the leading edge of the airfoil are higher than those at the trailing edge, where the lift is generated. The pressure coefficient (Cp) of the airfoil's upper surface was negative, and that of the lower surface was positive, indicating the lift generated on the wing, for both AoA.

The comparison of the pressure coefficient between the experiment and computational fluid dynamics (CFD) showed that the minimum Cp at 0° AoA was -0.6 from the experiment and -0.54 from the CFD. Although there was a slight variation in Cp at the leading edge between the experiment and CFD, major regions of the airfoil had a Cp matching between the experiment and simulation. Furthermore, the lift coefficient obtained from the Cp plot was found to be 0.203 from experiment and 0.215 from fluent. The difference in Cp at the leading edge could be attributed to experimental errors, which may include certain variations in AoA and wall effects in the wind tunnel. Moreover, the pressure coefficient obtained from the simulation lies well within the error bars of the experiment, suggesting that the experiment and simulation validate each other, thereby proving the working principle behind 3D printed pressure taps.

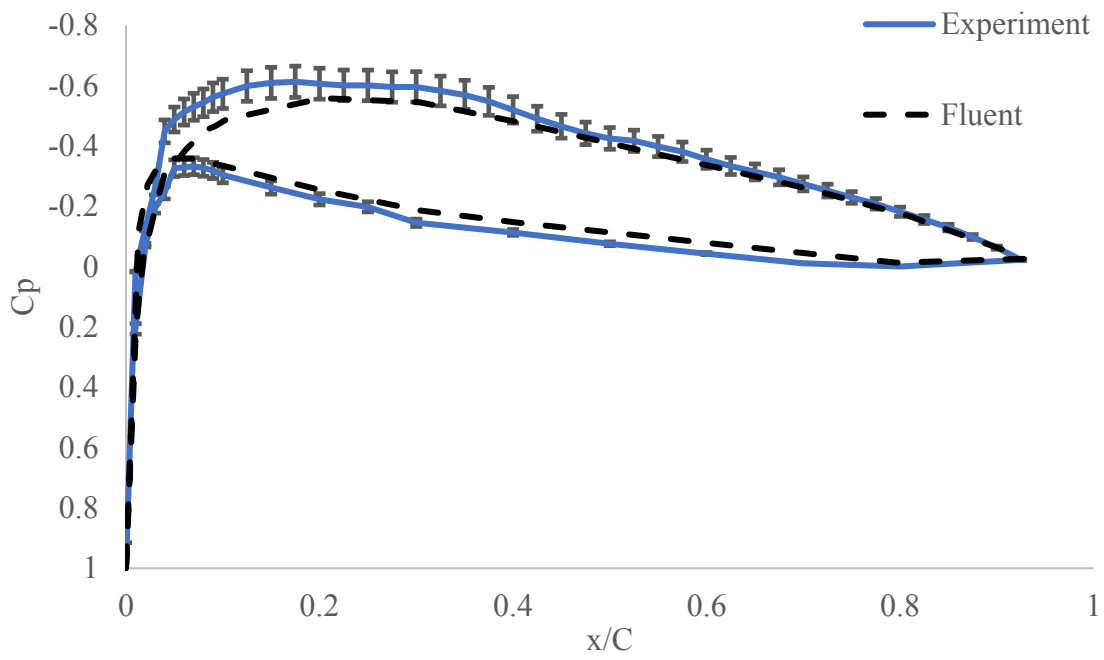

Figure 5-7: C_p validation plot for Re=6.54x10^5 at α=0°.

Similarly, the comparison of the pressure coefficient at 3° AoA showed a remarkable similarity between the experiment and CFD, with the Cp curve matching very well between them. The pressure at the leading edge dropped to a minimum of -0.83, indicating a rise in lift coefficient with increasing AoA. Furthermore, the lift coefficient obtained from the Cp plot was found to be 0.624 from experiment and 0.613 from fluent. The similarity between CFD and experiment supports the working principle of 3D printed pressure taps for pressure measurements. These findings highlight the reliability of the experimental method and the accuracy of the [30] 3D printed pressure taps in measuring pressure distribution on airfoils under various angles of attack.

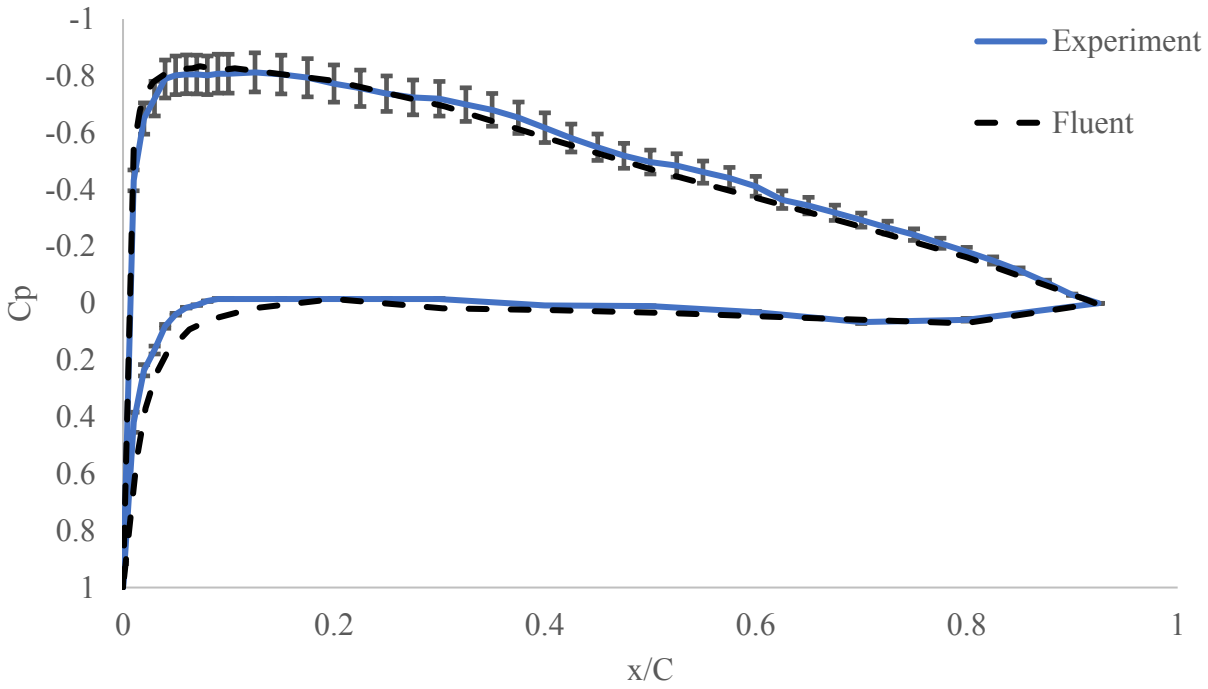

Figure 5-8: C_p validation plot for Re=6.54x10^5 at α=3°.

Table 5: Lift Coefficient between experiment and fluent.

AoA	Experiment (C_L)	Fluent (C_L)
0	0.203	0.215
5	0.624	0.613

5.3.2 Open Test Section Data

In this research, the focus was on investigating the performance of 3D printed pressure taps on the surface of an airfoil NACA 2412. The airfoil was tested in an open wind tunnel at various speeds ranging from 10 to 30 m/s and at angles of attack (AoA) of 0°, 5°, and 10°. The surface pressure measurement data followed the expected curve and matches well with the CFD simulations. Furthermore, the pressure coefficient plot reveals

the presence of laminar separation on the airfoil surface, particularly on the upper surface of the airfoil at higher angles of attack.

The experimental data showed that the pressure coefficient was positive near the leading edge, indicating that there was a region of low pressure there. The pressure coefficient decreased rapidly towards the maximum thickness point of the airfoil and then decreased more gradually towards the trailing edge. The CFD results showed similar trends but differed in magnitude, with the CFD pressure coefficient being generally lower than the experimental one. This discrepancy may be due to several factors, such as the modeling of turbulence or the boundary conditions used in the simulation. This discrepancy however is witining the range of 10% between experiment and simulation.

At 0° AoA, a small bump in Cp was observed at x/c = 0.8, which gradually moved towards x/c = 0.6 and 0.45 at 5° and 10° AoA, respectively as shown in Figure 5-9, Figure 5-10, and Figure 5-11. Around 4-8 pressure taps were around the region of separation to capture this effect. This bump in Cp was indicative of a trailing edge separation on the airfoil, where the flow separated from the airfoil surface due to adverse pressure gradient [30, 31]. The location of the separation point moved towards the leading edge as the AoA increased, indicating a greater extent of flow separation. The reason behind CFD not being able to capture the separation might be mainly due to turbulence modeling which adds turbulent viscosity to the flow. Furthermore, the lift coefficient obtained from the Cp plot was found to be 0.132, 0.646 and 1.845 for respective AoA from experiment and 0.13, 0.645 and 1.87 from fluent. Overall, the results are well within the error band and suggest that the 3D printed pressure taps were effective in detecting the presence of flow separation.

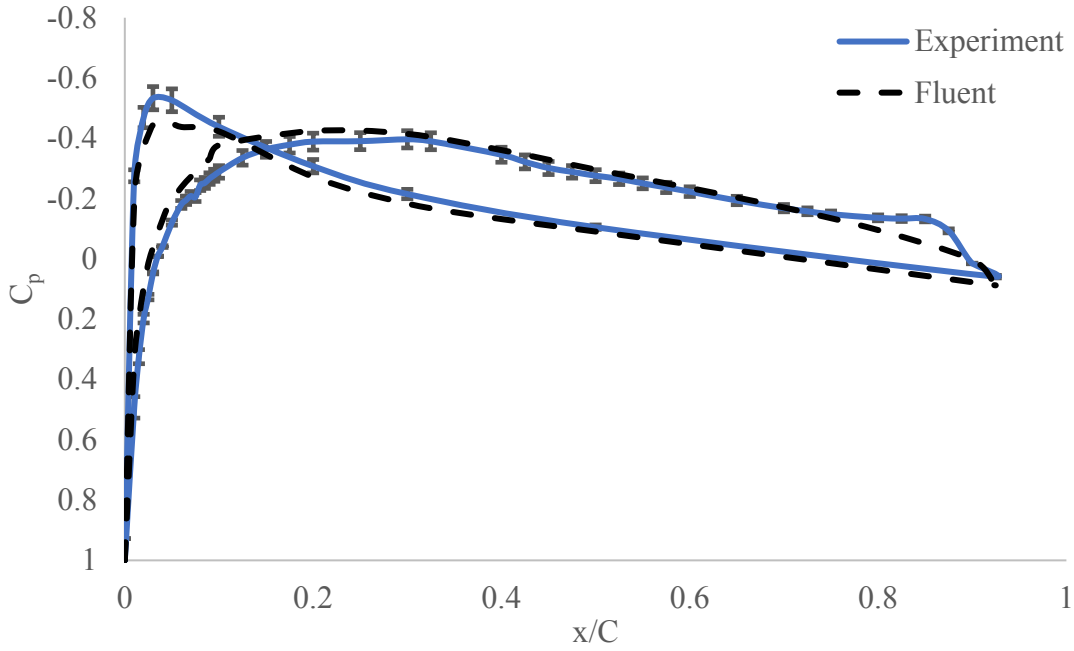

Figure 5-9: C_p validation plot for Re=2.1x10^5 at α=0°.

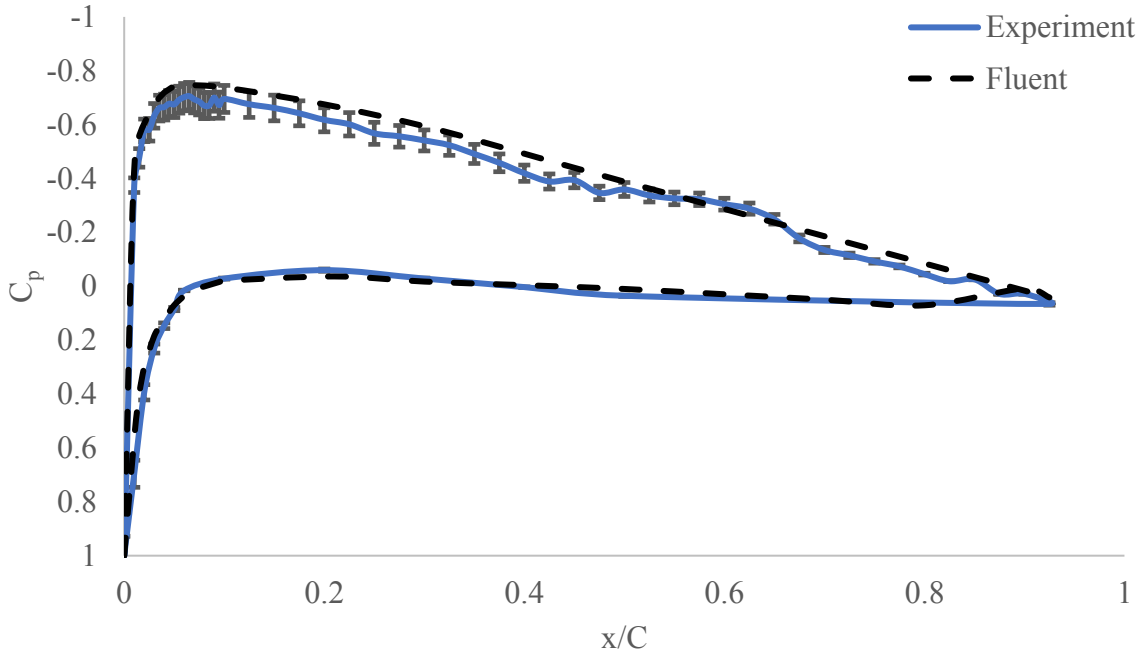

Figure 5-10: C_p validation plot for Re=2.1x10^5 at α=5°.

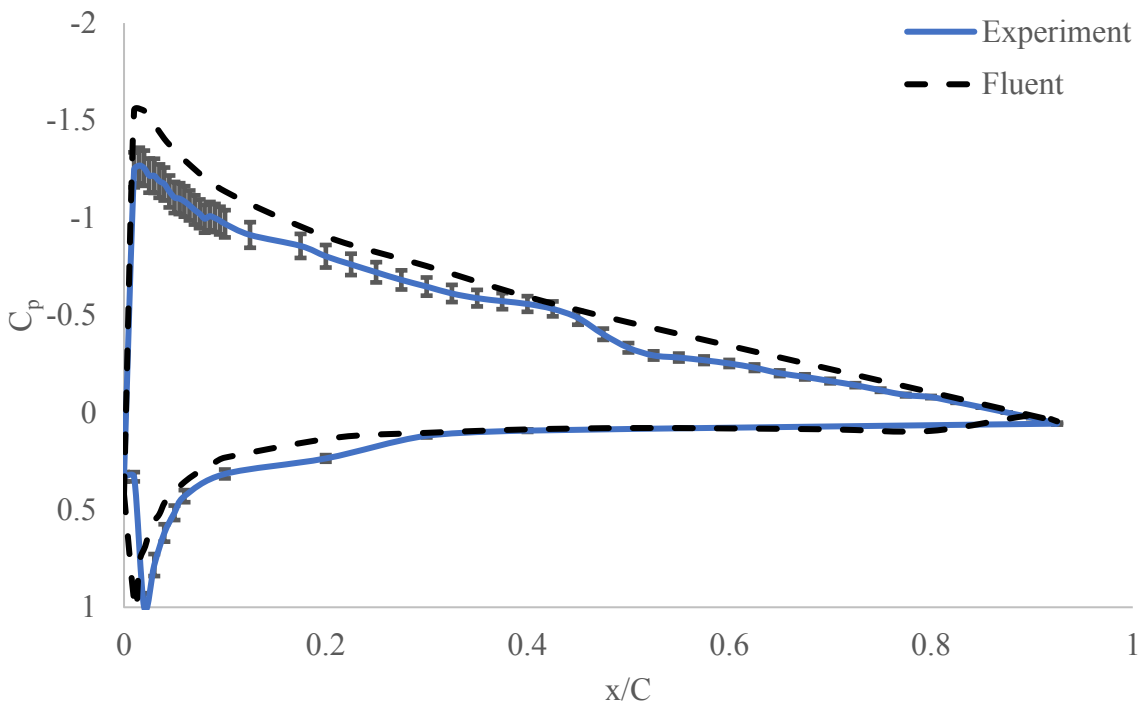

Figure 5-11: C_p validation plot for Re=2.1x10^5 at α=10°.

The 3D printed pressure taps were found to be highly effective in capturing the complex flow features around the airfoil. Even with the presence of vortical flows and turbulent wakes, the pressure taps were still able to accurately measure the surface pressure distribution. This was evidenced by the fact that the pressure coefficient plots showed clear and distinct changes in pressure along the surface of the airfoil, which corresponded with the expected flow features. The ability of the 3D printed pressure taps to capture these complex flow features demonstrates their usefulness in experimental fluid dynamics research.

Table 6: Lift coefficient between experiment and fluent.

AoA	Experiment (C_L)	Fluent (C_L)
0	0.132	0.13
5	0.646	0.645
10	1.845	1.87

Additionally, the pressure taps were able to capture the effects of the vortex generators that were installed on the airfoil. The reattachment of flow separation at x/c=0.8 was clearly evident in the pressure coefficient plots, which showed a significant reduction in the bump in Cp at all angles of attack. This indicates that the vortex generators were effective in controlling the flow separation and reducing the associated drag. It is to be noted that the pressure measurements were only obtained for the upper surface of the airfoil as no effects of VG would be seen on the bottom surface.

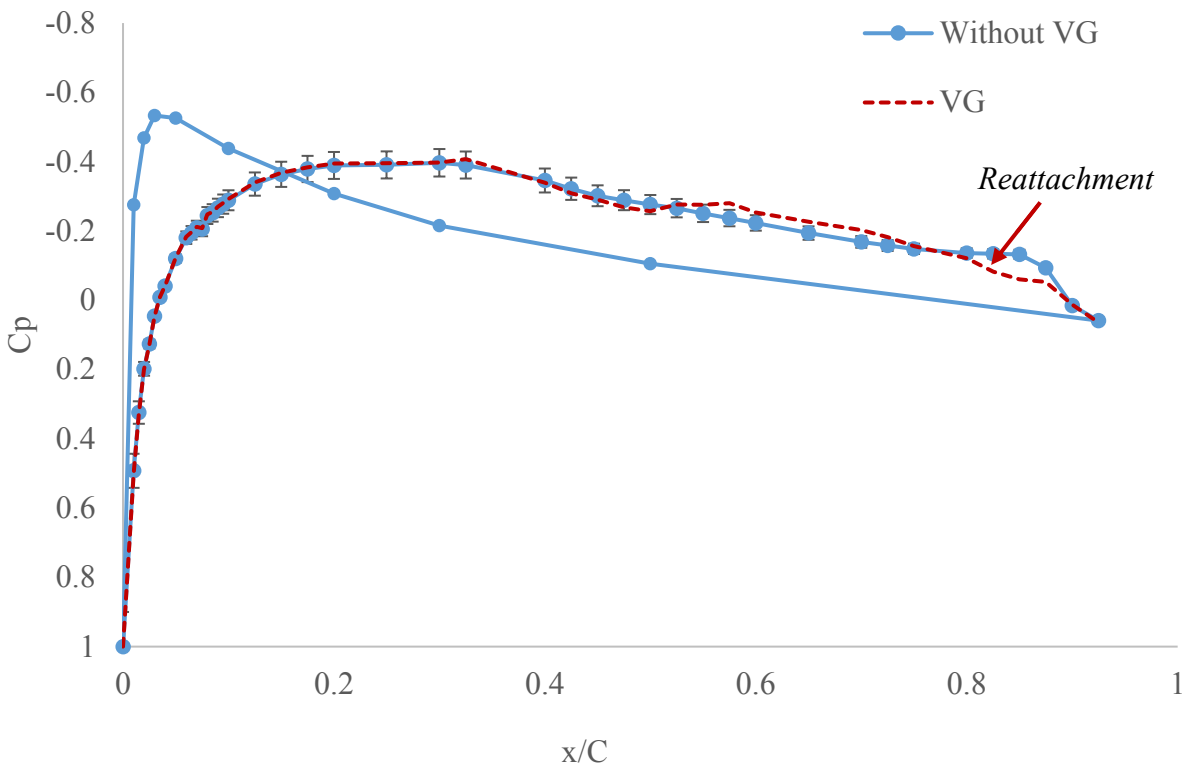

Figure 5-12: C_p plot with VGs for Re=2.1x10^5 at α=0°.

Moreover, the pressure taps utilized in the present study proved to be effective in capturing the alterations in the surface pressure distribution with the variation of angle of attack. Notably, as the angle of attack was progressively elevated from 0 to 10 degrees, the bump in Cp, was significantly reduced signifying reattached of the flow. This outcome is consistent with the anticipated behavior of a VG, which often reenergizes the flow and mitigates the adverse pressure gradients.

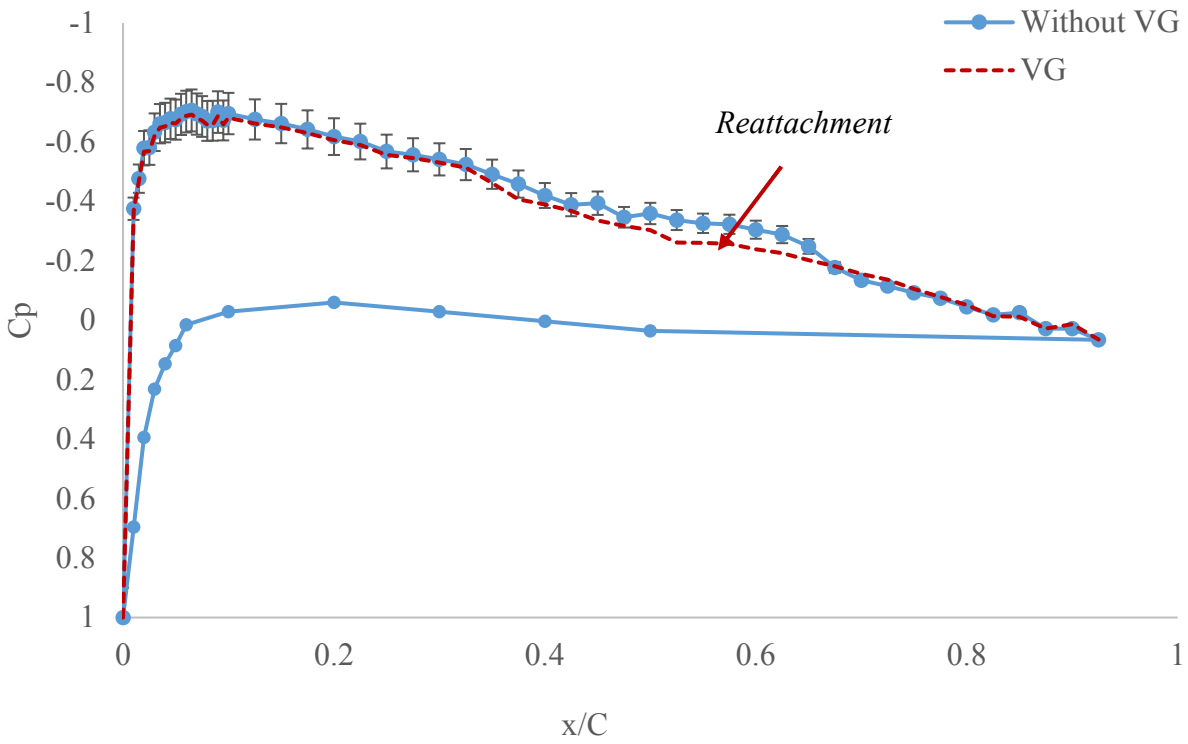

Figure 5-13: C_p plot with VGs for Re=2.1x10^5 at α=5°.

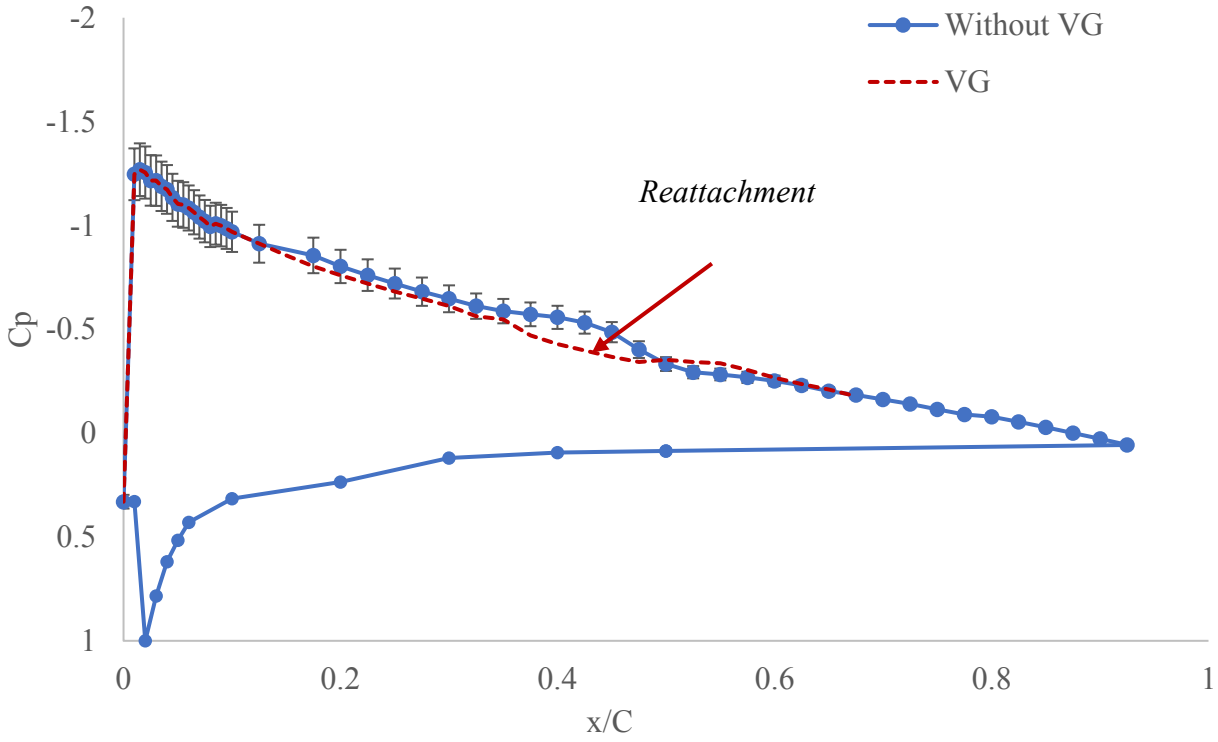

Figure 5-14: C_p plot with VGs for Re=2.1x10^5 at α=10°.

Overall, the 3D printed pressure taps proved to be a valuable tool in this study, allowing for the accurate measurement of the surface pressure distribution and the detection of complex flow features. Their use in combination with other experimental techniques such as flow visualization can provide a more complete understanding of the flow behavior around an airfoil.

CHAPTER 6. CONCLUSION

6.1 Conclusion

Based on the findings above, several key conclusions can be made regarding the effectiveness of pressure measurements from 3D printed pressure taps. These conclusions are as follows,

1. The comparison of pressure coefficient plots for the straight and complex pathed pressure taps cases showed good agreement, indicating that complex paths can serve as an alternative to traditional straight pathed pressure taps. However, some deviation was observed among these cases, which could be attributed to surface roughness differences and experimental errors. Furthermore, these deviations were still within the range of experimental error band.
2. The validation of the experimental results with literature values revealed a close agreement between the experimental and literature values, supporting the conclusion that the 3D printed cylinder used in the experiment is a suitable model for investigating the flow over a circular cylinder. The experimental and literature data also revealed the typical characteristics of the flow phenomenon over the cylinder, including a leading-edge separation and a gradual increase in pressure before the onset of vortex shedding.
3. The experimental findings showed good agreement with the computational fluid dynamics (CFD) simulation outcomes, indicating the efficacy of the 3D printed pressure taps in capturing complex flow features around the airfoil, including the effects of vortex generators installed on the airfoil.

4. The results of this study also demonstrate the efficacy of 3D printed pressure taps in measuring pressure across a wide range of Reynolds numbers, ranging from 4,000 to 600,000.

6.2 Future Works and Recommendations

The conclusions drawn from this study have implications for future research in the field of flow measurement and aerodynamics. To further investigate the deviation observed between the pressure coefficient plots for straight and complex pathed pressure taps, future experiments could focus on optimizing the surface roughness of the 3D printed pressure taps. This could involve exploring various surface finishes for the 3D prints and testing their effectiveness in reducing surface roughness. In addition, future research could also aim to improve the experimental setup to minimize external disturbances, such as wind gusts or vibrations, which can impact the accuracy of the pressure measurements. This could involve using a more stable mounting system or conducting experiments in a controlled wind tunnel environment. Furthermore, the potential of 3D printing technology to produce complex shapes with embedded pressure taps could be further explored for investigating flow behavior over other complex geometries, such as airfoils with intricate shapes and morphing capabilities or geometries where traditionally manufactured pressure taps are hard to obtain. In these cases, the design and printing of pressure taps with specific shapes and orientations could allow for the capture of the complex flow features around such geometries, providing valuable insights for the development of aerodynamic devices for various applications.

References

[1] W. Zhu, "Models for Wind Tunnel Tests Based on Additive Manufacturing Technology," *Progress in Aerospace Sciences ,* 2019.

[2] A. Springer, "Evaluating Aerodynamic Characteristics of Wind-Tunnel Models Produced by Rapid Prototyping Methods," *Journal of Spacecraft and Rockets,* vol. 35, no. 6, 1998.

[3] A. L. Heyes and D. A. R. Smith, "Rapid Technique for Wind-Tunnel Model Manufacture," *Journal of Aircraft,* vol. 41, no. 2, pp. 413-415, 2004.

[4] R. J. Hildebrand and R. C. Eidson, "Development of a Low Cost, Rapid Prototype, Lambda Wing-Body Wind Tunnel Model," in *21st Applied Aerodynamics Conference*, Orlando, Florida, 2003.

[5] D. A. Gebbie, M. F. Reeder, C. Tyler, V. Fonov and J. Crafton, "Lift and Drag Characteristics of a Blended-Wing Body Aircraft," *Journal of Aircraft,* vol. 44, no. 5, 2007.

[6] C. Aghanajafi and S. Daneshmand, "Integration of Three-Dimensional Printing Technology," *Journal of Aircraft,* vol. 47, no. 6, 2010.

[7] M. R. Blanco, "Design and Qualification of a Boundary-Layer Wind Tunnel for Modern CFD Validation Experiments," Master's Thesis OhioLINK Electronic Theses and Dissertations Center, 2019.

[8] T. Bykerk, "Tiertime," 30 August 2018. [Online]. Available: https://www.tiertime.com/sydney-researcher-3d-prints-for-hypersonic-aircraft-testing/. [Accessed Feburary 2023].

[9] Z. Zhou and D. Li, "Design and fabrication of a hybrid surface-pressure airfoil model based on rapid prototyping," *Rapid Prototyping Journal,* vol. 14, no. 1, pp. 57-66, 2008.

[10] C. Tyler, W. Braisted and J. Higgins, "Evaluation of Rapid Prototyping Technologies for Use in Wind Tunnel Model Fabrication," in *43rd AIAA Aerospace Sciences Meeting and Exhibit*, Reno, Nevada, 2005.

[11] S. Shun and N. A. Ahmed, "Rapid Prototyping of Aerodynamics Research Models," *Applied Mechanics and Materials,* Vols. 217-219, pp. 2016-2025, 2012.

[12] M. Moioli, C. Reinbold, K. Sorensen and C. Breitsamter, "Investigation of Additively Manufactured Wind Tunnel Models with Integrated Pressure Taps and Vortex Flow Analysis," *Aerospace,* vol. 6, no. 10, 2019.

[13] A. Gatto, K. P. Byrne, N. A. Ahmed and R. D. Archer, "Meand and Fluctuating Pressure Measurements Over a Circular Cylinder in Cross Flow Using Plastic Tubing," *Experiments in Fluids ,* vol. 30, pp. 43-46, 2001.

[14] A. D. Cutler and P. Bradshaw, "Strong Vortex/Boundary Layer Interactions," *Experiements in Fluids,* vol. 14, pp. 321-332, 1993.

[15] O. Lögdberg, J. Fransson and P. Alfredsson, "Streamwise evolution of longitudinal vortices in a turbulent boundary layer," *Journal of Fluid Mechanics,* 2009.

[16] C. Yao, J. C. H. Lin and B. Allan, "Flow-Field Measurement of Device-Induced Embedded Streamwise Vortex on a Flat Plate," in *NTRS - NASA Technical Reports Server*, 2002.

[17] I. M. M. A. Shabaka, R. D. Mehta and P. Bradshaw, "Longitudinal vortices imbedded in turbulent boundary layers. Part 1. Single vortex," *Journal of Fluid Mechanics,* vol. 155, pp. 37-57, 1985.

[18] S. Arunvinthan, V. Raatan, S. N. Pillai, A. A. Pasha, M. M. Rahman and K. A. Juhany, "Aerodynamic Characteristics of Shark Scale-Based Vortex Generators upon Symmetrical Airfoil," *Energies,* vol. 14, no. 7, 2021.

[19] H. Hatoum and L. P. Dasi, "Reduction of pressure gradient and turbulence using vortex generators in prosthetic heart valves," *Ann Biomed Eng.,* vol. 47, no. 1, pp. 85-96, Jan 2019.

[20] J. C. Lin, "Review of research on low-profile vortex generators to control boundary-layer separation," *Progress in Aerospace Sciences,* vol. 38, no. 4-5, pp. 389-420, 2002.

[21] L. Florentie, "Aspects of Source-Term Modeling for Vortex-Generator Induced Flows," Delft University of Technology Docotral Thesis, 2018.

[22] "Guide to Stereolithography (SLA) 3D Printing," Formlabs, [Online]. Available: https://formlabs.com/blog/ultimate-guide-to-stereolithography-sla-3d-printing/. [Accessed 14 March 2023].

[23] M. Drela, "XFOIL: An Analysis and Design System for Low Reynolds Number Airfoils," in *Low Reynolds Number Aerodynamics*, Berlin, Springer, 1989, pp. 1-12.

[24] P. Parnaudeau, J. Carlier, D. Heitz and E. Lamballais, "Experimental and numerical studies of the flow over a circular cylinder at Reynolds number 3900," *Physics of Fluids,* vol. 20, no. 8, 2008.

[25] M. E. Young and A. Ooi, "Comparative Assessment of LES and URANS for Flow Over a Cylinder at a Reynolds of 3900," in *16th Australasian Fluid Mechanics Conference*, Crown Plaza, Gold Coast, Australia, 2-7 December 2007 .

[26] C. Norberg and B. Sunden, "Turbulence and reynolds number effects on the flow and fluid forces on a single cylinder in cross flow," *Journal of Fluids and Structures,* vol. 1, no. 3, pp. 337-357, July 1987.

[27] E. Douvi, D. P. Margaris and T. I. Athanasios, "Evaluation of the turbulence models for the simulation of the flow over a National Advisory Committee for Aeronautics (NACA) 0012 airfoil," *Journal of Mechanical Engineering Research,* vol. 4, no. 3, March 2012.

[28] G. Jones, J. Lin, B. Allan, W. Milholen, C. Rumsey and R. Swanson, "Overview of CFD Validation Experiments for Circulation Control Applications at NASA," in *NTRS - NASA Technical Reports Server*, London, July 22, 2008.

[29] S. K. NUNES, "PERFORMANCE OF A DUAL PLANE AIRFOIL MODEL WITH VARYING GAP, STAGGER, AND DECALAGE USING PRESSURE MEASUREMENTS AND PARTICLE IMAGE VELOCIMETRY," Master's Thesis OhioLINK Electronic Theses and Dissertations Center, 2021.

[30] J. Winslow, H. Otsuka, B. Govindarajan and I. Chopra, "Basic Understanding of Airfoil Characteristics at Low Reynolds Numbers (104–105)," *Journal of Aircraft,* vol. 55, no. 3, May 2018.

[31] A. Crivellini, V. D'Alessandro, D. D. Benedetto, S. Montelpare and R. Ricci, "Study of laminar separation bubble on low Reynolds number operating airfoils: RANS modelling by

means of an high-accuracy solver and experimental verification," in *Journal of Physics*, 2014.

[32] A. Springer and K. Cooper, "Comparing The Aerodynamic Characteristics of Wind Tunnel Models Produced By Rapid Prototyping And Conventional Methods," in *15th AIAA Applied Aerodynamics Conference*, 1997.

[33] K. Olasek and P. Wiklak, "Application of 3D Printing Technology in Aerodynamic Study," in *Journal of Physics*, 2014.

Appendix

Table 7: Coordinates for pressure taps.

	x/c	X (m)	Y (m)
1	0	0	0
2	0.01	0.002286	0.004064
3	0.015	0.003429	0.00508
4	0.02	0.004572	0.005842
5	0.025	0.005715	0.00635
6	0.03	0.006858	0.007112
7	0.035	0.008001	0.00762
8	0.04	0.009144	0.008128
9	0.045	0.010287	0.008636
10	0.05	0.01143	0.009144
11	0.055	0.012573	0.009398
12	0.06	0.013716	0.009906
13	0.065	0.014859	0.01016
14	0.07	0.016002	0.010668
15	0.075	0.017145	0.010922
16	0.08	0.018288	0.01143
17	0.085	0.019431	0.011684
18	0.09	0.020574	0.011938
19	0.095	0.021717	0.012192

20	0.1	0.02286	0.012446
21	0.125	0.028575	0.013716
22	0.15	0.03429	0.014732
23	0.175	0.040005	0.015494
24	0.2	0.04572	0.016256
25	0.225	0.051435	0.016764
26	0.25	0.05715	0.017272
27	0.275	0.062865	0.017526
28	0.3	0.06858	0.017526
29	0.325	0.074295	0.01778
30	0.35	0.08001	0.01778
31	0.375	0.085725	0.017526
32	0.4	0.09144	0.017526
33	0.425	0.097155	0.017272
34	0.45	0.10287	0.017018
35	0.475	0.108585	0.01651
36	0.5	0.1143	0.016256
37	0.525	0.120015	0.015748
38	0.55	0.12573	0.01524
39	0.575	0.131445	0.014732
40	0.6	0.13716	0.014224
41	0.625	0.142875	0.013462

42	0.65	0.14859	0.012954
43	0.675	0.154305	0.012192
44	0.7	0.16002	0.01143
45	0.725	0.165735	0.010668
46	0.75	0.17145	0.009906
47	0.775	0.177165	0.009144
48	0.8	0.18288	0.008128
49	0.825	0.188595	0.007366
50	0.85	0.19431	0.00635
51	0.875	0.200025	0.005334
52	0.9	0.20574	0.004318
53	0.925	0.211455	0.003302
54	0.01	0.002286	0.00381
55	0.02	0.004572	0.00508
56	0.03	0.006858	0.005842
57	0.04	0.009144	0.006604
58	0.05	0.01143	0.007112
59	0.06	0.013716	0.008382
60	0.1	0.02286	0.00889
61	0.2	0.04572	0.009906
62	0.3	0.06858	0.009906
63	0.4	0.09144	0.009144

64	0.5	0.1143	0.008128

Table 8: Pressure measurement for 0 AoA

	x/c	P (psi)
1	0	0.01878
2	0.01	0.00925
3	0.015	0.00609
4	0.02	0.00372
5	0.025	0.00238
6	0.03	0.00087
7	0.035	-0.0002
8	0.04	-0.0008
10	0.05	-0.0023
12	0.06	-0.0034
13	0.065	-0.0037
14	0.07	-0.0039
15	0.075	-0.0039
16	0.08	-0.0046
17	0.085	-0.0047
18	0.09	-0.005
19	0.095	-0.0052
20	0.1	-0.0054
21	0.125	-0.0063
22	0.15	-0.0068

23	0.175	-0.0071
24	0.2	-0.0073
26	0.25	-0.0073
28	0.3	-0.0074
29	0.325	-0.0073
32	0.4	-0.0065
33	0.425	-0.006
34	0.45	-0.0057
35	0.475	-0.0054
36	0.5	-0.0052
37	0.525	-0.005
38	0.55	-0.0047
39	0.575	-0.0045
40	0.6	-0.0042
42	0.65	-0.0036
44	0.7	-0.0032
45	0.725	-0.003
46	0.75	-0.0028
48	0.8	-0.0026
49	0.825	-0.0025
50	0.85	-0.0025
51	0.875	-0.0017

52	0.9	0.00029
53	0.925	0.00111
	0.925	0.00111
	0	0.01878
54	0.01	-0.0052
55	0.02	-0.0088
56	0.03	-0.01
57	0.05	-0.0099
58	0.1	-0.0082
59	0.2	-0.0058
60	0.3	-0.004
61	0.5	-0.002
	0.925	0.00111